ESD-TR-87-028
ESL-TR-85-039

Final Report

Laser Remote Sensing of Atmospheric Pollutants

30 September 1985

Lincoln Laboratory

MASSACHUSETTS INSTITUTE OF TECHNOLOGY

LEXINGTON, MASSACHUSETTS

Prepared for the Air Force
under Electronic Systems Division Contract F19628-85-C-0002.

The work reported in this document was performed at Lincoln Laboratory, a center for research operated by Massachusetts Institute of Technology. This work was supported by the Department of the Air Force under Contract F19628-85-C-0002, in part with specific funding from the Engineering and Services Laboratory, Air Force Engineering and Services Center, Tyndall Air Force Base, Florida.

This technical report has been reviewed and is approved for publication.

FOR THE COMMANDER

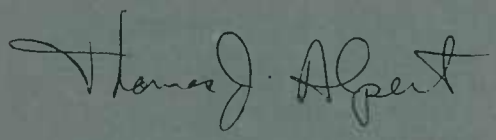

Thomas J. Alpert, Major, USAF
Chief, ESD Lincoln Laboratory Project Office

MASSACHUSETTS INSTITUTE OF TECHNOLOGY
LINCOLN LABORATORY

LASER REMOTE SENSING OF ATMOSPHERIC POLLUTANTS

D.K. KILLINGER
N. MENYUK
A. MOORADIAN
Group 82

FINAL REPORT
TO THE
AIR FORCE ENGINEERING AND SERVICES CENTER

1 OCTOBER 1984 — 30 SEPTEMBER 1985

ISSUED 21 JULY 1987

LEXINGTON MASSACHUSETTS

ABSTRACT

This FY85 Final Report on the program entitled "Laser Remote Sensing of Atmospheric Pollutants" covers the period 1 October 1984 to 30 September 1985. The work was supported by the Air Force Engineering and Services Center.

TABLE OF CONTENTS

LIST OF ILLUSTRATIONS

LASER REMOTE SENSING OF ATMOSPHERIC POLLUTANTS

I. INTRODUCTION

This is the FY85 Final Report on the program entitled "Laser Remote Sensing of Atmospheric Pollutants" supported by the Air Force Engineering and Services Center.

The specific tasks which were conducted during FY85 for this research program consisted of the following:

(a) The continuation of the Co:MgF_2 DIAL measurement of atmospheric species, and

(b) Initial remote sensing demonstration of a HCl plume in the atmosphere.

Each of these tasks is described in detail in the following sections. Supportive documentation is included in the appendices.

II. Co:MgF_2 DIAL MEASUREMENTS OF ATMOSPHERIC SPECIES

The Co:MgF_2 laser differential-absorption lidar (DIAL) system reported in the FY84 Final Report* was modified in order to increase laser output power and to incorporate a better telescope; Figures 1 and 2 show photographs of the Co:MgF_2 laser and DIAL system. These modifications enhanced the lidar signal sufficiently so that returns from atmospheric aerosols were easily observable. As a result, range-resolved laser remote sensing measurements of the atmosphere were made using this system and were used to establish detection range and sensitivity. The technical details of the laser system have been presented in the FY84 Final Report, and details of the DIAL experiments and related investigations are given in Appendices A and B. A synopsis of the study is given below.

The Co:MgF_2 DIAL system had sufficient laser power (10 mJ/pulse) and optical detection sensitivity to permit the remote sensing of lidar backscatter from aerosols and molecules in the atmosphere. Figure 3 shows a plot of the Co:MgF_2 lidar returns from atmospheric aerosols as a function of range. As seen in the figure, lidar returns were recorded at ranges out to 3.8 km, with significant signal-to-noise ratios measured at ranges out to about 3 km. These results are in good agreement with theoretical calculations which predicted that the Co:MgF_2 DIAL system should be capable of detecting atmospheric backscatter returns out to ranges of ~3 to 4 km (see Appendix A).

---

* D.K. Killinger, N. Menyuk, and A. Mooradian, "Laser Remote Sensing of the Atmosphere," FY84 Final Report, Lincoln Laboratory, MIT, ESD-TR-85-212, ESL-TR-85-34 (30 September 1984), DTIC AD-A159531/3.

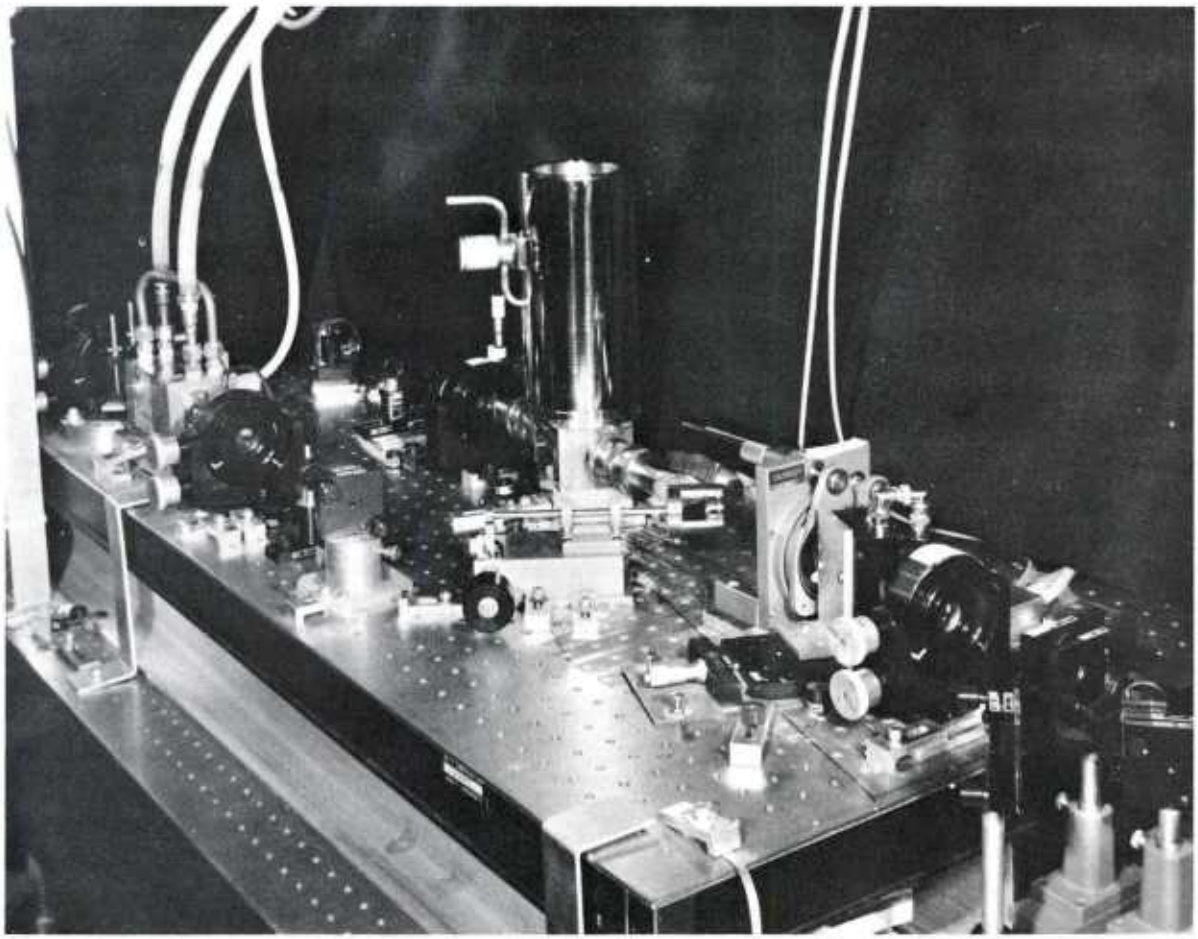

80485-1

Figure 1. Photograph of Co:MgF_2 laser.

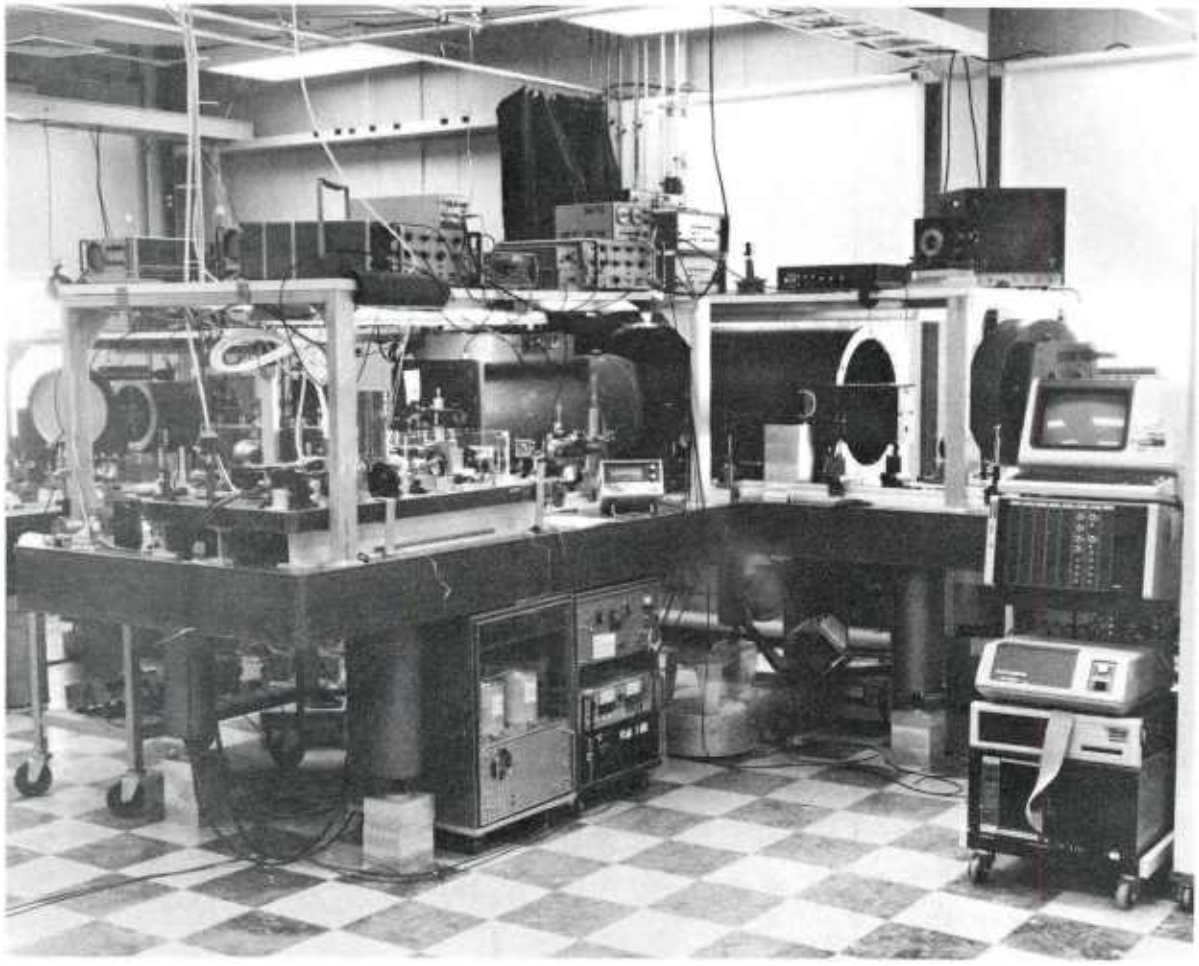

80485-2

Figure 2. Photograph of Co:MgF_2 DIAL system.

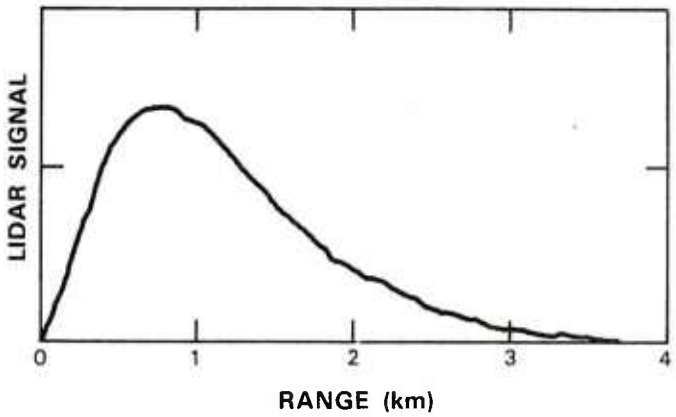

77093-1

Figure 3. Range-resolved Co:MgF_2 lidar returns backscattered from atmospheric aerosols as a function of range.

III. REMOTE SENSING OF HCl PLUME

The Co:MgF_2 DIAL system, operating near 1.7525 μm, was used for the range-resolved remote sensing of HCl in the atmosphere. Previous DIAL experiments (FY84 Final Report) had established that a negligible amount of ambient HCl (<0.2 ppm) was present in the atmosphere. Therefore, an artificial source of HCl was used in order to provide a plume of HCl suitable for remote sensing. In order to reduce the amount of gaseous HCl injected into the atmosphere, a semi-enclosed cell was used. The 1-m-long, 0.8-m-diam., windowless cell was placed at a distance of 200 m from the DIAL system, and the 0.3-m-diam. lidar beam passed unobstructed through the cell. Figure 4 shows the normalized lidar signal obtained after HCl was injected into the cell.

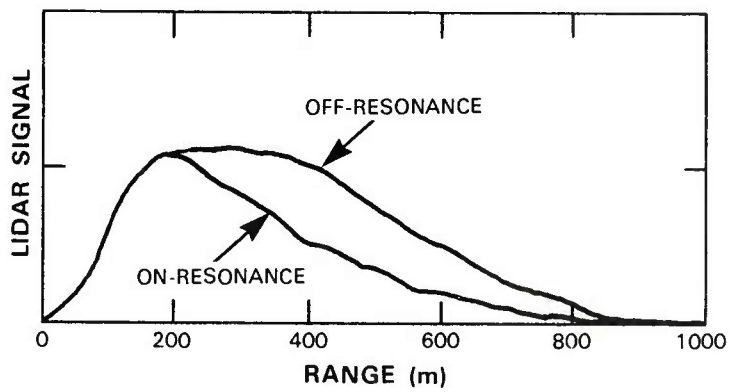

77093-2

Figure 4. Differential-absorption (range-resolved) remote sensing of HCl plume. The lidar beam passed through a semi-enclosed cell at a range of 200 m which contained the source of the HCl plume.

The difference between the on-line and off-line signals indicates that ~40 ppm of HCl was present. The minimum differential-absorption signal observable was a few percent of this value. As such, we estimate that the sensitivity of the Co:MgF_2 DIAL system was ~1 to 3 ppm with a 200-m range resolution. The range resolution is determined by the laser pulse length and, as seen in the figure, is responsible for the considerable degree of spatial averaging seen in the data. A shorter pulse length of the Co:MgF_2 laser would permit a shorter range resolution to be obtained.

IV. COMPARISON OF EXPERIMENTAL DATA WITH PREDICTIONS

One can compare the experimental results shown in Figure 4 with the theoretical predictions of the sensitivity of the Co:MgF_2 DIAL system. The predictions are presented in Figures 5 and 6 which show the calculated minimum detectable concentration of atmospheric HCl as a function of range for both path-averaged and range-resolved measurements assuming a laser pulse energy of 10 mJ; details of the calculations are given in Appendix A.

Figure 5 indicates that the system should be capable of detecting path-averaged concentrations of HCl between 0.1 and 1 ppm over ranges to about 10 km. This prediction is in good

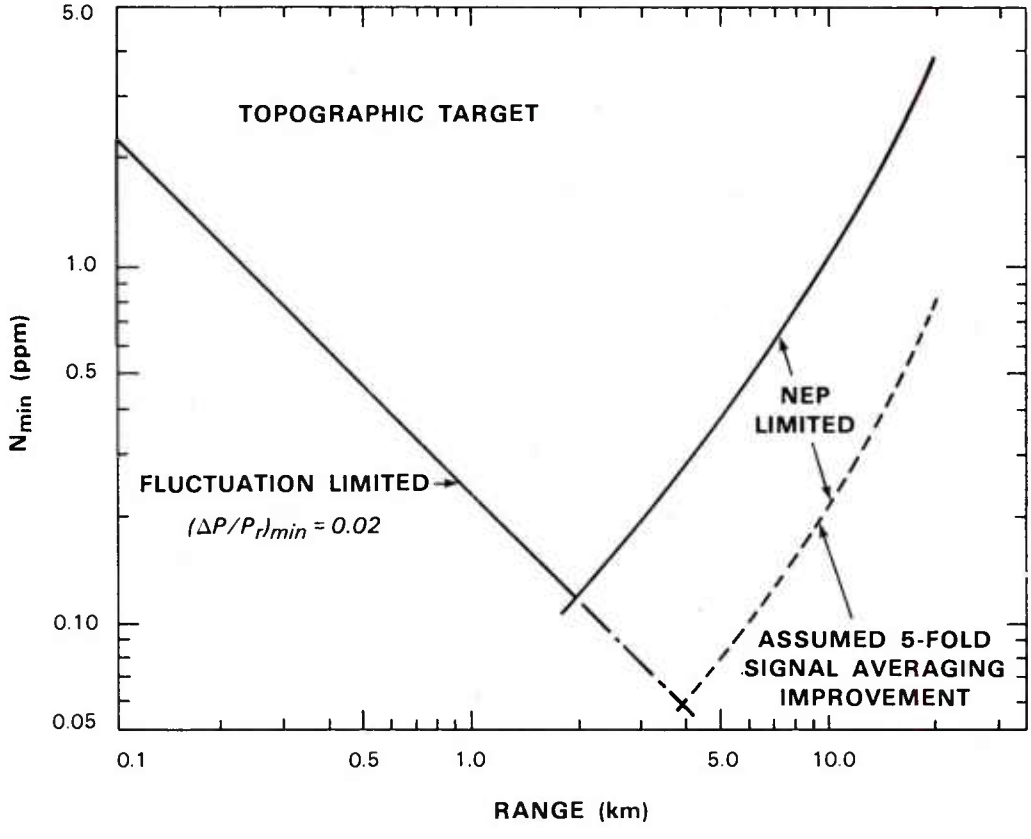

77337-2

Figure 5. Predicted detection range for path-averaged remote sensing of HCl in the atmosphere.

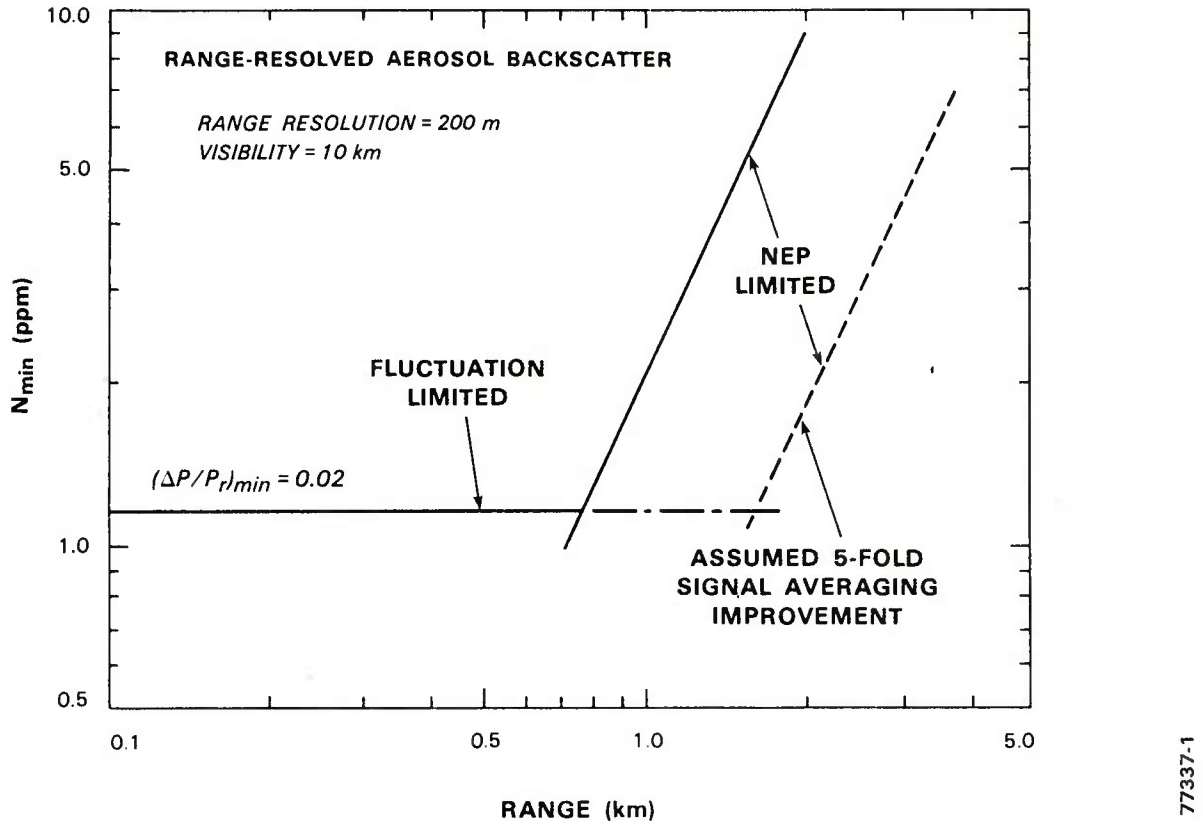

Figure 6. Predicted detection range for range-resolved remote sensing of HCl in the atmosphere.

agreement with the experimental data which indicated a sensitivity on the order of 0.2 ppm and detection ranges out to 6 km (see Appendix A).

The range-resolved aerosol backscatter predictions shown in Figure 6 indicate that a concentration sensitivity of a few pulses per million to a range of ~2 km may reasonably be expected. These predictions are in good agreement with the experimental data shown in Figure 4.

V. ASSOCIATED PROGRAMS IN Co:MgF_2 LASER DEVELOPMENT

The detection range of the Co:MgF_2 DIAL system, while certainly adequate for many remote sensing applications, could be enhanced by increasing the output power of the Co:MgF_2 laser. The current laser is limited in energy to ~10 mJ/pulse because of optical damage to the laser cavity mirrors; at higher Q-switched powers, the dichroic mirror is irreversibly damaged. Several studies have been made by others to increase the power out of the Co:MgF_2 laser.

Sanders Associates* has recently completed a program funded by AFSC/Wright Patterson Avionics Laboratory to develop a high-power Co:MgF_2 laser. This program recently demonstrated 30-Hz pulsed laser operation at the peak of the Co:MgF_2 gain (1.9 μm) of 0.5 J/pulse in the long-pulsed (non-Q-switched) mode and 150 mJ/pulse in a 150-ns Q-switched pulse. Higher powers were limited by optical damage to the cavity mirrors.

Finally, it should be noted that the Co:MgF_2 laser is currently being investigated also by Schwartz Electro-Optics† with funding from NASA/Langley. This program has demonstrated operations of the Co:MgF_2 laser at 0°C using a thermoelectric cooler instead of liquid nitrogen cooling for the Co:MgF_2 crystal.

VI. CONCLUSION

The Co:MgF_2 DIAL system has been shown to be useful for path-averaged and range-resolved remote sensing of atmospheric species at ranges up to 6 and 3 km, respectively. Range-resolved DIAL measurements of HCl plumes have established a detection sensitivity of a few parts per million and indicate that the Co:MgF_2 DIAL system can be useful for the detection of a wide variety of HCl gaseous sources in the atmosphere. Future developments related to enhancing the output power of the Co:MgF_2 laser should certainly increase the detection range and sensitivity of the DIAL system.

---

* M. Thomas, Sanders Associates (private communication).

† P. Moulton, Schwartz Electro-Optics (private communication).

APPENDIX A

The following is a reprint of a journal article accepted for publication in Applied Optics, entitled "Atmospheric Remote Sensing of Water Vapor, HCl and CH_4 Using a Continuously Tunable Co:MgF_2 Laser."

ATMOSPHERIC REMOTE SENSING OF WATER VAPOR, HCl AND CH_4 USING A CONTINUOUSLY TUNABLE Co:MgF_2 LASER

N. Menyuk and D.K. Killinger
Lincoln Laboratory, Massachusetts Institute of Technology
Lexington, MA 02173-0073

ABSTRACT

A differential-absorption lidar (DIAL) system has been developed which uses a continuously tunable (1.5 — 2.3 μm) cobalt-doped magnesium fluoride (Co:MgF_2) laser as the radiation source. Preliminary atmospheric measurements of water vapor, HCl and CH_4 have been made with this system, including both path-averaged and range-resolved DIAL measurements at ranges up to 6 km and 3 km, respectively.

* This work was supported by the National Aeronautics and Space Administration and the Air Force Engineering and Services Center.

I. INTRODUCTION

There is an acknowledged need for tunable high-power lasers in the near-to middle-IR to serve as sources in lidar systems for remote sensing of the atmosphere.[1] Recently several new IR lasers which show potential for use as sources for lidar or differential-absorption lidar (DIAL) systems have been developed. They include optical parameteric oscillators (OPO) pumped by a Nd:YAG laser,[2] Ti:Al_2O_3 lasers,[3] and OH:NaCl lasers.[4]

The solid-state, cobalt-doped magnesium fluoride laser (Co:MgF_2),[5,6] which is continuously tunable from 1.5 to 2.3 μm, also falls in this category. In this paper we report on the adaptation and use of a Co:MgF_2 laser as a practical pulsed source of coherent radiation in a DIAL system and describe the use of this system to measure atmospheric species in the atmosphere. The system can produce either path-averaged or range-resolved remote sensing measurements to ranges of 6 km and 3 km, respectively.

II. Co:MgF_2 DIAL SYSTEM

The DIAL system is described in this section. In addition to the Co:MgF_2 laser, the system includes optical diagnostics for energy and spectral monitoring of the laser, lidar optics consisting of a beam steering mirror, receiving telescope, and optical detector, and a computer to record the DIAL signals and to control and monitor the laser wavelength. A schematic of the complete system is given in Figure 1.

A. Co:MgF_2 Laser

Early investigations of the Co:MgF_2 laser by Moulton[5] established that the laser was continuously tunable from 1.5 to 2.3 μm, could operate either cw or pulsed, and could radiate at a single frequency. Lovold *et al.*[6] modified the original design so that the laser could be Q-switched and accurately controlled in wavelength in order to make the Co:MgF_2 laser a practical radiation source for remote sensing measurements. The resulting configuration is shown in the upper left portion of Figure 1.

The Co:MgF_2 laser was longitudinally pumped by a 1.32 μm Nd:YAG laser which emitted 400 mJ, 800 μs duration, linearly polarized, multimode pulses at a 3 Hz pulse repetition frequency. The pump pulse was focused onto a 27 mm long Co:MgF_2 crystal cut at the Brewster angle. The crystal was mounted in a liquid nitrogen Dewar which, in turn, had entrance and exit windows set at the Brewster angle. The output coupling mirror (M2 in Figure 1) used for the remote sensing measurements reported here had a 95% reflectivity at 1.7 μm, and the dichroic back mirror (M1 in Figure 2) had high reflectivity at 1.7 μm and high transmission at 1.32 μm. An intracavity, fused-silica, acousto-optic Q-switch was used to reduce the laser pulse length to 300 ns; when operated in a free-running, pulsed mode (non-Q-switched), the output appears as a series of spikes spaced approximately 50 μs apart and covering a time span of about 300 μs, making that operative mode difficult to use for remote sensing application.

Course tuning and linewidth control of the the laser was obtained using a three-element birefringent tuning filter[6] which reduced the linewidth to approximately 1 cm^{-1} and permitted laser tuning over the spectral range from 1.6 to 1.9 μm, the maximum range obtainable with a single set of laser cavity mirrors. A quartz intracavity etalon, 0.25 mm thick and coated for 20% reflectivity, reduced the linewidth to 0.15 cm^{-1} and was angle tuned for precision scanning of the laser wavelength over a limited range of the order of 5 cm^{-1}. The output energy of the Co:MgF_2 laser was limited to approximately 10 mJ when operated Q-switched in order to avoid optical damage to the dichroic mirror.

B. DIAL System

As seen in Figure 1, the bulk of the Co:MgF_2 laser output is used for remote sensing, but portions of the output are sampled using beamsplitters to provide diagnostics. In particular, a room temperature HgCdTe detector[7] monitors the energy of each pulse and provides an optical trigger to various components, and the 1-m long absorption cell shown in the figure permits laboratory calibration of the absorption of the molecule being investigated as a function of the laser wavelength. The spectrometer shown monitors the laser frequency at a particular position; however, when the laser is used in a continous frequency scanning mode, the fixed air-gap Fabry-Perot gives an accurate measure of the laser wavelength variation, which is fed directly to the computer. In addition, the spectrometer is used as a spectrograph, with the output imaged on a 64-element pyroelectric detector array with 100 μm spacing of the individual elements. This arrangement permits visual observation in real time of the laser wavelength output over a range of about 25 cm^{-1} to ensure that the output is a single mode of the intracavity etalon and is continuously tuning over the free spectral range of the etalon.

The remote sensing portion of the output beam is expanded to a 3 cm diameter and is directed to the target with a 50 cm beam steering mirror. The return lidar beam is sent through a 30 cm Cassegrain telescope and detected by a cooled InSb detector. The output signal is then measured by an A/D converter or a waveform digitizer and analyzed by the computer. The computer also controls and scans the wavelength of the laser by use of a Burleigh "Inchworm" which changes the slant angle of the thin etalon in the laser cavity.

The system can run the wavelength control of the laser either in a continuous scanning mode, or in a differential-absorption (DIAL) mode. In this latter case only two wavelengths, on and off an absorption line, are employed and the position of the etalon is toggled between these two positions. In the continuous scanning mode, the output of the Fabry-Perot is used to calibrate the relative wavelength of the laser and to correctly scale the wavelength scan of the laser and lidar returns.

III. PATH-AVERAGED DIAL MEASUREMENTS

The system has been operated in the continuous scanning mode to obtain path-averaged (column content) measurements using backscattered returns from topographic targets. Figure 2

shows a plot of the normalized lidar returns obtained from foliage on hillsides located 3 km and 6.7 km from the laboratory as a function of the laser wavelength. The wavelength scan covers approximately 5 cm^{-1}. All the major absorption regions can be identified with known water vapor absorption lines.[8-10] While more than one absorption line is involved in most of the transition regions, the absorption near 1.7678 μm is primarily due to a single H_2O transition with an absorption linewidth equal to 0.11 cm^{-1} at atmospheric pressure and an expected peak absorption coefficient, σ_a, of 5.2×10^4 $(atm\text{-}cm)^{-1}$.[8] One deduces from the observed absorption strength of 52% in Figure 2(a) that approximately 0.0023 atmospheres (1.8 Torr) of water vapor was present in the atmosphere.

This DIAL measurement can be compared to that obtained using a wet-bulb/dry-bulb thermometer which indicated a 0.0048 atmospheres (3.7 Torr) of water vapor and an ambient temperature of 7°C. As evident, the DIAL deduced value was a factor of 2 less than the actual experimental conditions indicated. This discrepancy is attributable to the finite linewidth of the Co:MgF_2 laser (0.15 cm^{-1}) in comparison to the water vapor linewidth, which serves to reduce the peak absorption strength and to broaden the measured absorption line, as seen in Figure 2. Cahen and Megie[11] have considered this problem assuming Gaussian lineshapes. They found that for laser linewidths approximately equal to the absorption linewidth, deviations in the observed absorption strength of the order of 30% may be expected, and that the deviation increases with increasing laser linewidth and integrated optical density. It is clear that under experimental conditions in which these effects are significant, accurate molecular concentration determination can only occur when such an effect has been calibrated or when the laser linewidth is significantly narrower than the molecular absorption linewidth.

Frequency scans have also been made over spectral regions containing absorption lines of the 2.0 band of HCl and the $2\nu_3$ band of CH_4. During the scan, simultaneous measurements were made of the return signal from the hillside 3 km distant and the transmittance of the laser beam passing through an absorption cell 1-m in length containing a known concentration of either HCl or CH_4. The results of such a simultaneous measurement with 15 Torr of HCl in air at atmospheric pressure in the absorption cell are shown in Figure 3. The frequency scan in Figure 3 covers 2.3 cm^{-1} and encompasses the 1.7525 μm R(1) line of the 2-0 band of HCl. The upper section of Figure 3 corresponds to an R(1) absorption coefficient of 0.43 $(atm\text{-}cm)^{-1}$. The remote sensing data obtained simultaneously and shown in the lower portion of Figure 3 shows the presence of nearby water vapor lines, but within experimental uncertainty there is little indication HCl ($<$0.2 ppm) in the atmosphere between the hillside and the laboratory; the experimental accuracy was primarily limited by uncertainty in the background signal level shown in Figure 3(b), which led to an error of approximately 5%.

A similar measurement was carried out over the spectral region which included the 1.6713 μm P(2) absorption line of the $2\nu_3$ band of CH_4. The laboratory measurement indicated an absorption coefficient of 0.036 $(cm\text{-}atm)^{-1}$ for this line, and no ($<$2 ppm) CH_4 was detected in the atmosphere.

IV. RANGE RESOLVED AEROSOL DIAL MEASUREMENTS

The Co:MgF_2 DIAL system has sufficient transmitted laser energy and optical detection sensitivity to measure the lidar backscatter from natural oecurring aerosols in the atmosphere, and thereby provides the capability of detecting the range-resolved concentration of various species in the atmosphere. As an example, Figure 4 shows the lidar signal, averaged over 50 pulses, as a function of range for atmospheric backscatter. As seen, the Co:MgF_2 DIAL system is capable of detecting aerosol backscatter at ranges out to 3.8 km, with significant signal levels at ranges of 0.2 to 3 km.

Preliminary experiments using the range-resolved Co:MgF_2 DIAL system were conducted in order to assess its capabilities for atmospheric studies. Figure 5 shows a 25 pulse average of the range resolved lidar returns as the laser was tuned on- and off-resonance through a strong water vapor line near 1.7515 μm with an expected absorption coefficient of 8.3×10^{-3} $(atm\text{-}cm)^{-1}$; this strong absorption line of H_2O was chosen to enhance the differential absorption at close ranges. One deduces from the observed differential signal near 300 m in Figure 5 that approximately 1.7 Torr of water vapor was present. This value differs significantly from the 2.5 Torr value measured using a wet-bulb/dry-bulb thermometer. The difference is similar to that observed in the path-averaged measurements (Figure 2) and, as in that case, the deviation is presumably due to the finite linewidth of the laser. Calibration errors in the assumed absorption strengths of the water vapor lines and background continuum may also be contributing to this effect.

The Co:MgF_2 DIAL system was also used to detect HCl in the atmosphere under range-resolved conditions. Since the background concentration of HCl in the atmosphere is too small to be measurable, artificial means of injecting a plume of HCl into the atmosphere was used. In order to reduce the total amount of gaseous HCl injected into the atmosphere, a semi-enclosed cell was used. The 1-m long, 0.8-m diameter, window-less cell was placed at a distance of 200 m and the 0.3-m diameter lidar beam passed unobstructed through the cell. Figure 6 shows the normalized lidar signal obtained after HCl was injected into the cell. The difference between the on-line and off-line signals indicates that approximately 40 ppm of HCl was present over the 200-m range resolution of the system. The range resolution is determined by the laser pulse length and, as seen in the figure, is responsible for the considerable degree of spatial averaging seen in the data. A shorter pulse length of the Co:MgF_2 laser would permit a shorter range resolution to be obtained.

V. DIAL MEASUREMENT SENSITIVITY

It is of interest to calculate the theoretical measurement sensitivity of the Co:MgF_2 DIAL system. The sensitivity of a differential absorption remote sensing system is determined by the minimum change in the signal return which can be detected. The ultimate sensitivity at far ranges occurs when this minimum observable change, ΔP, is equal to the noise equivalent power (NEP) of the detection system. In that case, for measurements of signal returns from a target located at

a range R, the minimum average detectable average concentration over the distance to the target is given, for small absorption, by[12]

$$N_{min} \simeq \frac{(NEP)\ \pi R}{2\rho\sigma_a AKP_t \exp(-2\alpha R)} \quad , \tag{1}$$

where ρ is the target reflectivity, σ_a is the absorption coefficient of the molecule being investigated, A is the telescope area, K is the optical efficiency of the system, P_t is the transmitted power, and α is the atmospheric absorption exclusive of the investigated molecule. For the case of range-resolved aerosol backscatter, σ_a is replaced with $\sigma_a \Delta R/R$ and the target reflectivity, ρ, is replaced with $\beta \Delta R$, where ΔR is the range resolution of the lidar and β is the aerosol backscatter coefficient.

At close in ranges, N_{min} is further limited by fluctuations in the return signals to the minimum fractional change of those signals, $\Delta P/P_r$, which can be detected; P_r is the returned lidar power. In that case, for hard target backscatter,[12]

$$N_{min} = \frac{(\Delta P/P_r)}{2\sigma_a R} \quad . \tag{2}$$

To estimate the sensitivity of the present Co:MgF_2 system for the column content measurement of HCl on the basis of Eqs. (1) and (2), the parameters used were: NEP = 1.5×10^{-9} W, $\rho = 0.1$, $\sigma_a = 0.43$ (cm-atm)$^{-1}$, K = 0.1, A = 0.125 m^2, $P_t = 3 \times 10^4$ W, and $\alpha = 0.03$ km^{-1}. The resulting values of N_{min} as a function of range are shown in Figure 7, where it is assumed that signal averaging will reduce the minimum measurable $\Delta P/P_r$ to 2% and will produce a 5-fold improvement in sensitivity in the (NEP)-limited region. Improvement of this magnitude is well within the capability of signal averaging for both path-averaged[13] and range-resoloved measurements.[14] The number of pulses required to achieve a five-fold reduction of the standard deviation will vary with atmospheric conditions, pulse-repetition frequency and wavelength, but would normally be expected to occur after averaging over the order of 50 to 100 pulses. The figure indicates that the system should be capable of detecting path averaged concentrations of HCl between 0.1 and 1 part per million over ranges to about 10 km using a 10 mJ pulse energy.

Figure 8 shows the results of a similar analysis carried out for range-resolved aerosol measurements; in this case β was estimated from the relationship $\beta = (0.017/V)$ m^{-1} sr^{-1},[15] where V is the visibility in meters, and assumed to be 10 km. As seen in Figure 8, the results indicate that a concentration sensitivity of a few parts per million to a range of approximately 2 km may reasonably be expected.

A calculation of the sensitivity of the Co:MgF_2 DIAL system for the remote sensing of CH_4 is similar to that shown above, except that the concentration detection sensitivity of CH_4 is approximately an order of magnitude smaller than that shown for HCl in Figures 7 and 8 due to a correspondingly smaller absorption coefficient, σ_a, for CH_4. In this case, one should be able to measure CH_4 concentrations of 10 to 100 parts per million, which could be useful for detecting and measuring gas leaks.

VI. CONCLUSIONS

The Co:MgF_2 laser, which is continuously tunable between 1.5 and 2.3 μm, has been shown to be a useful coherent radiation source for the remote sensing of atmospheric constituents with absorption lines in this spectral region. The Co:MgF_2 remote sensing system has functioned both in a mode in which it was continuously tuned through absorption lines of H_2O, HCl and CH_4, and in a differential absorption mode operating on and off the resonance frequency of an H_2O absorption line. While the remote sensing experiments did not observe any atmospheric HCl or CH_4, calculations indicate that the present system should be capable of detecting atmospheric HCl and CH_4 at concentrations of the order of 1 and 10 parts per million, respectively.

Acknowledgment

We want to thank Peter Moulton and Stian Lovold for help in the initial design and construction of the Co:MgF_2 laser and W. DeFeo for technical assistance in the taking of the DIAL data.

REFERENCES

1. D.K. Killinger and N. Menyuk, Science 235, 37 (1987).
2. Y.X. Fan, R. C. Eckardt, R.L. Byer, R.K. Route, and R.S. Feigelson, Appl. Phys. Lett. 45, 313 (1984).
3. P.F. Moulton, J. Opt. Soc. Am B3, 125 (1986).
4. J.E. Pinto, E. Georgiou, C.R. Pollock, Opt. Lett. 11, 519 (1986).
5. P.F. Moulton, IEEE J. Quantum Electron. QE-18, 1185 (1982).
6. S. Lovold, P.F. Moulton, D.K. Killinger and N. Menyuk, IEEE J. Quantum Electron. QE-21.
7. This detector was provided by D.L. Spears.
8. W.S. Benedict and R.F. Calfee, "Line Parameters for the 1.9 and 6.3 Micron Water Vapor Bands", Environmental Sci. Serv. Adm., ESSA Professional Paper 2, Washington, D.C. (1967).
9. L.S. Rothman, Appl. Opt. 20, 791 (1981). (This paper describes available AFGL atmospheric line parameter compilation.)
10. R.A. McClatchey, R.W. Fenn, J.E.A. Selby, F.E. Volz and J.S. Garing, "Optical Properties of the Atmosphere", Environmental Res. Paper No. 411 (1972).
11. C. Cahen and G. Megie, J. Quant. Spectrosc. Radiat. Transfer 12, 151 (1981).
12. D.K. Killinger and N. Menyuk, IEEE J. Quantum Electron. QE-17, 1917 (1981).
13. N. Menyuk, D.K. Killinger and C.R. Menyuk, Appl. Opt. 24, 118 (1985).
14. W. Staehr, W. Lahmann and C. Weitkamp, Appl. Opt. 24, 1950 (1985).
15. D.J. Brassington, Appl. Opt. 21, 4411 (1982).

FIGURE CAPTIONS

Fig. 1. Schematic of Co:MgF_2 DIAL system.

Fig. 2. Lidar returns backscattered from a hillside as a function of the Co:MgF_2 laser wavelength; The absorption features are due to water vapor in the atmosphere.

Fig. 3. Wavelength scan of Co:MgF_2 DIAL system showing both lidar returns and laboratory absorption cell signals as the laser wavelength was scanned over an absorption line of HCl. No HCl was measured in the atmosphere.

Fig. 4. Range-resolved Co:MgF_2 lidar returns from atmospheric aerosols as a function of range.

Fig. 5. Atmospheric range-resolved lidar returns as the Co:MgF_2 laser was tuned on- and off-resonance to the absorption line of water vapor near 1.7515 μm.

Fig. 6. Atmospheric range-resolved DIAL measurements of HCl injected into a semi-enclosed cell located at a range of 200 m

Fig. 7. Calculated path-averaged sensitivity of the Co:MgF_2 DIAL system for the remote sensing of atmospheric HCl.

Fig. 8. Calculated range-resolved sensitivity of the Co:MgF_2 DIAL system for the remote sensing of atmospheric HCl.

The views expressed are those of the author and do not reflect the official policy or position of the U.S. Government.

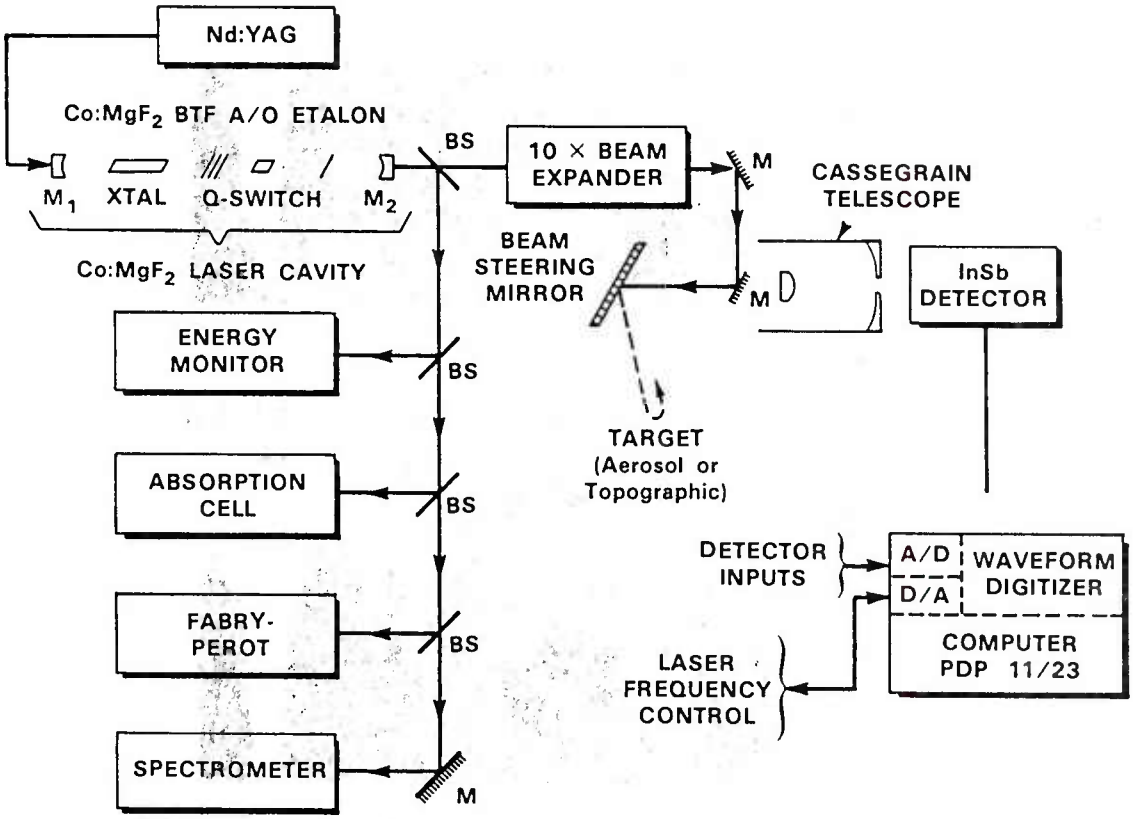
Nd:YAG
Co:MgF2 BTF A/O ETALON
M1
XTAL
Q-SWITCH
M2
Co:MgF2 LASER CAVITY
BS
10 × BEAM EXPANDER
M
CASSEGRAIN TELESCOPE
BEAM STEERING MIRROR
M
D
InSb DETECTOR
ENERGY MONITOR
BS
TARGET (Aerosol or Topographic)
ABSORPTION CELL
BS
DETECTOR INPUTS
A/D
D/A
WAVEFORM DIGITIZER
FABRY-PEROT
BS
COMPUTER PDP 11/23
LASER FREQUENCY CONTROL
SPECTROMETER
M

Figure 1.

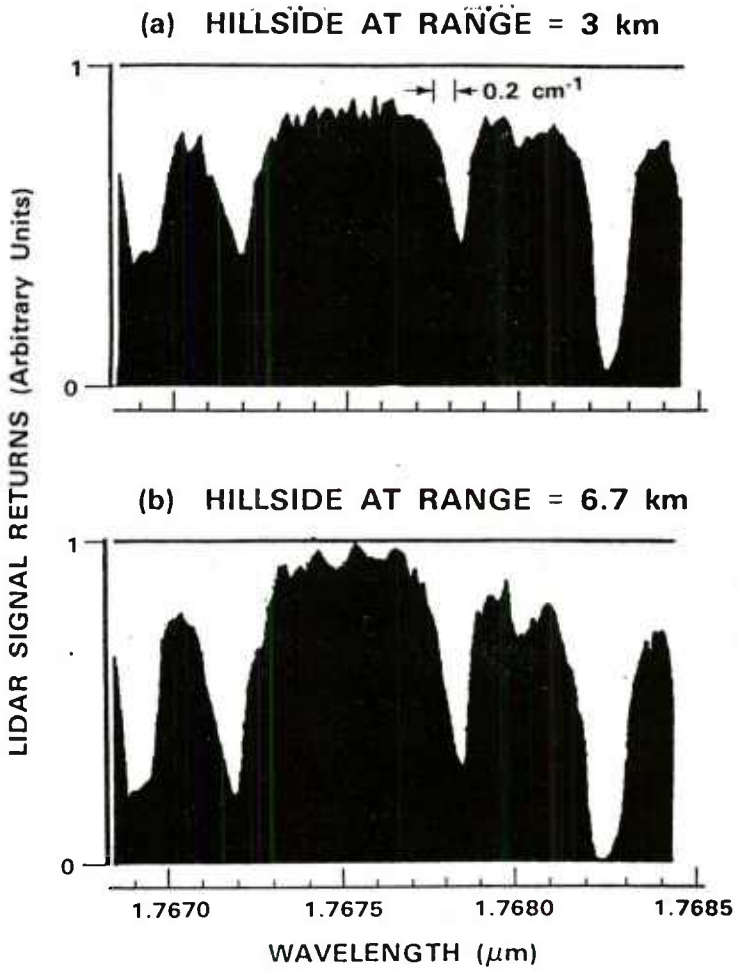
(a) HILLSIDE AT RANGE = 3 km
1
0
0.2 cm⁻¹
(b) HILLSIDE AT RANGE = 6.7 km
1
0
LIDAR SIGNAL RETURNS (Arbitrary Units)
1.7670
1.7675
1.7680
1.7685
WAVELENGTH (μm)

Figure 2.

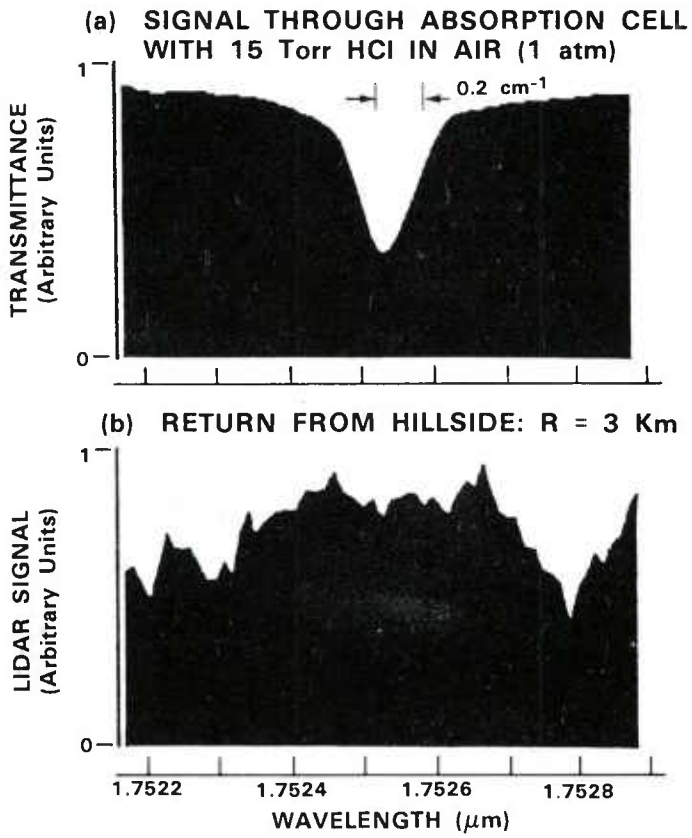
(a) SIGNAL THROUGH ABSORPTION CELL
WITH 15 Torr HCl IN AIR (1 atm)
0.2 cm-1
TRANSMITTANCE
(Arbitrary Units)
1
0
(b) RETURN FROM HILLSIDE: R = 3 Km
LIDAR SIGNAL
(Arbitrary Units)
1
0
1.7522
1.7524
1.7526
1.7528
WAVELENGTH (μm)

Figure 3.

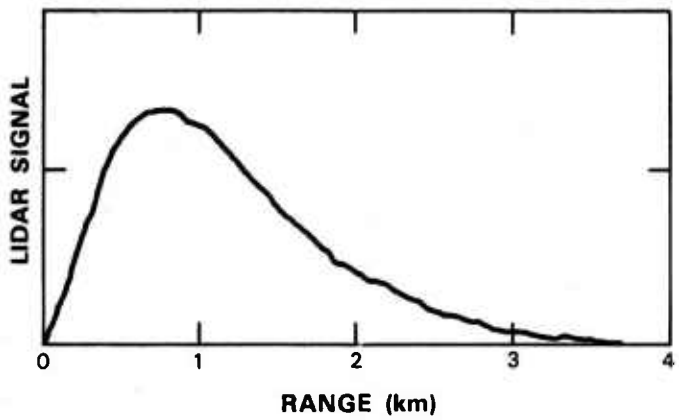

Figure 4.

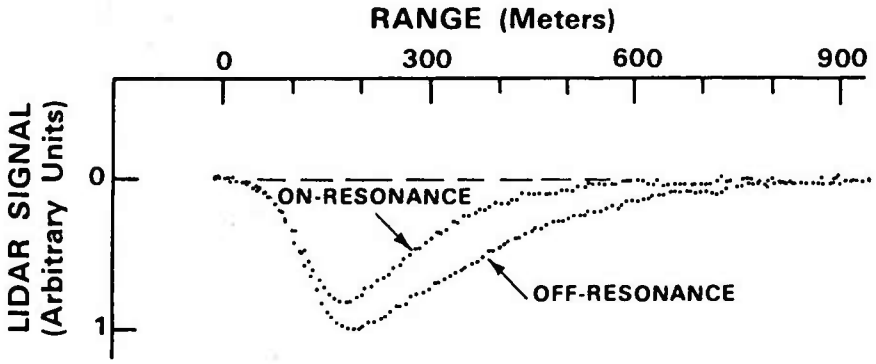

Figure 5.

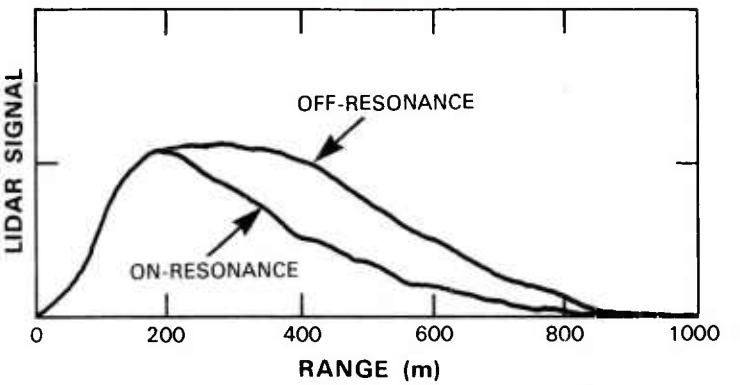

Figure 6.

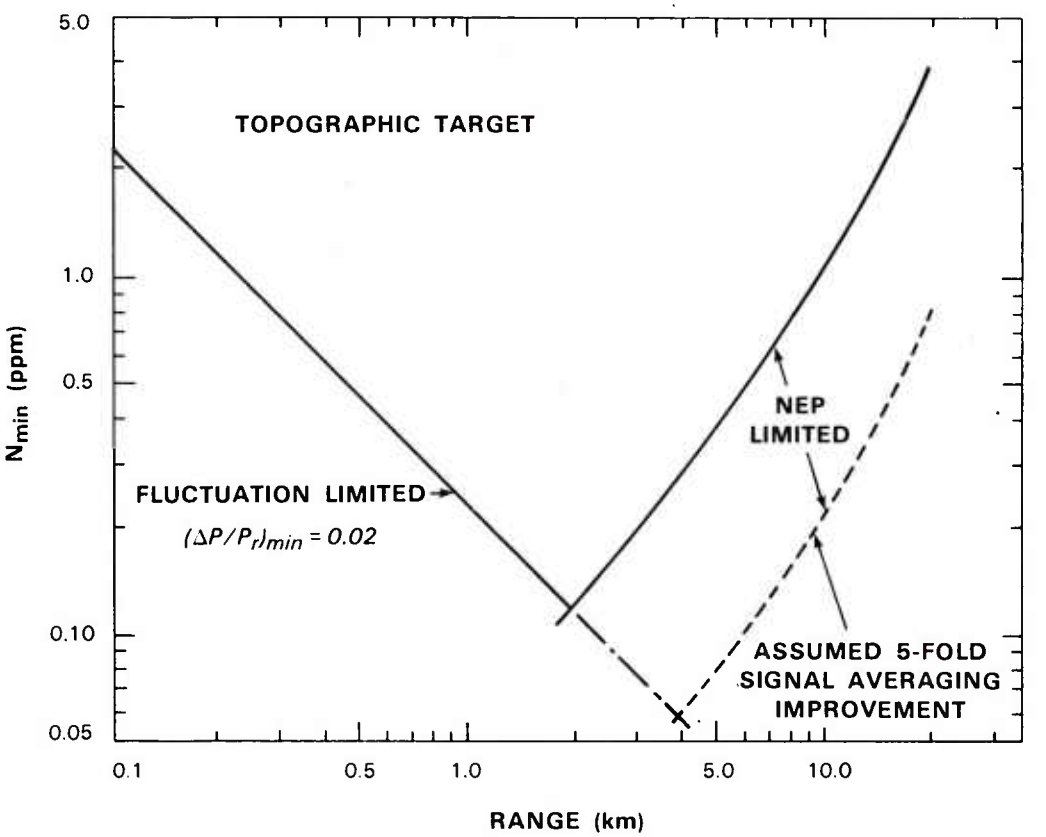

Figure 7.

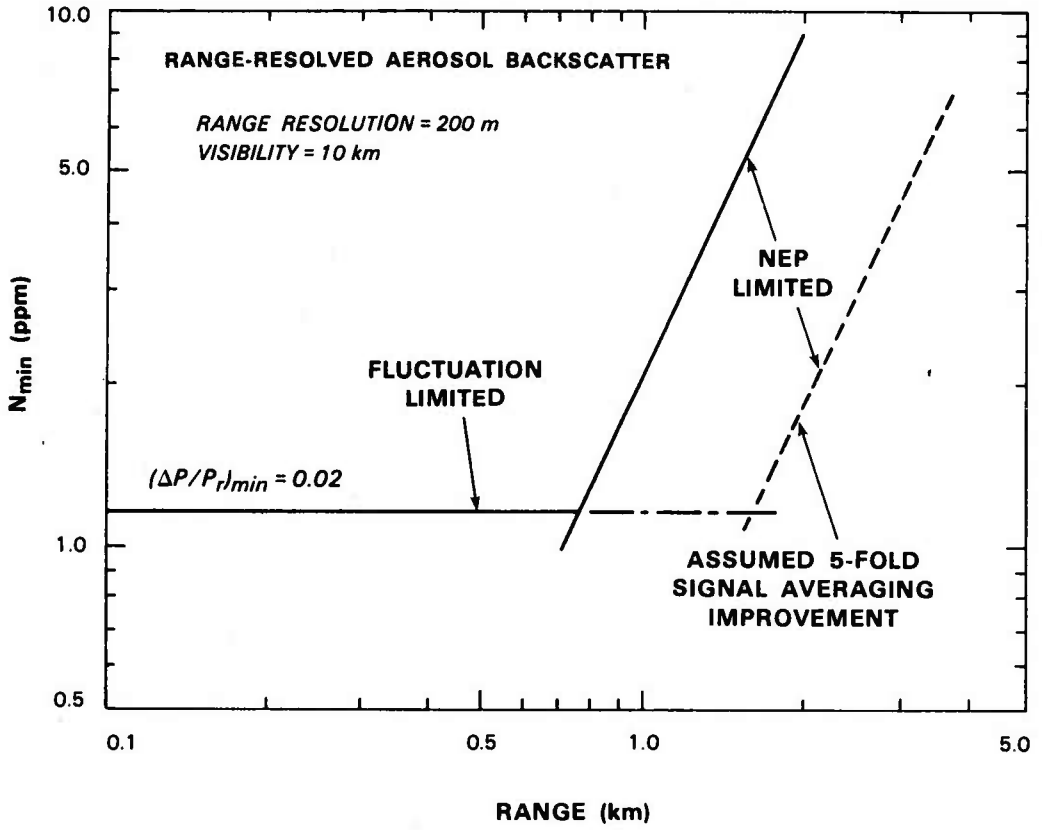
10.0
5.0
1.0
0.5
0.1
0.5
1.0
5.0
RANGE-RESOLVED AEROSOL BACKSCATTER
RANGE RESOLUTION = 200 m
VISIBILITY = 10 km
NEP
LIMITED
FLUCTUATION
LIMITED
(ΔP/Pr)min = 0.02
ASSUMED 5-FOLD
SIGNAL AVERAGING
IMPROVEMENT
Nmin (ppm)
RANGE (km)

Figure 8.

APPENDIX B

The following is a reprint of a journal article published in IEEE Journal of Quantum Electronics, March 1985, entitled "Frequency Tuning Characteristics of a Q-Switched Co:MgF_2 Laser."

Frequency Tuning Characteristics of a *Q*-Switched Co:MgF_2 Laser

S. LØVOLD, P. F. MOULTON, D. K. KILLINGER, AND N. MENYUK

Abstract—A tunable *Q*-switched Co:MgF_2 laser has been developed for atmospheric remote sensing applications. Frequency tuning is provided by a quartz etalon and a specially designed three-element birefringent filter covering the whole gain bandwidth of the Co:MgF_2 laser. The laser has good temporal and spectral characteristics, with an emission linewidth of approximately 3 GHz (0.1 cm^{-1}).

I. Introduction

THE strong coupling between electronic energy levels and the lattice in various transition-metal doped crystals has permitted the development of lasers tunable over broad frequency regions in the near infrared. The first such laser to be demonstrated was the Ni-doped MgF_2 laser by Johnson *et al.* in 1963 [1]. Later, laser pumping of Ni-, Co- and V-doped MgF_2 crystals greatly improved the performance of these so-called "vibronic" lasers [2]-[6]. The Co:MgF_2 laser is one of the most promising among these because it has negligible excited state absorption and can be tuned from 1.6 to 2.3 μm. CW, *Q*-switched, and mode-locked operation has been demonstrated, with up to 80 percent quantum efficiency [3]-[6].

The gain curve of the Co:MgF_2 laser has several sharp peaks at pure electronic transitions, as seen in Fig. 1. The peak gain cross section is relatively low, 1.5×10^{-21} cm^2 [7]. Thus the precise tuning of the laser across the gain bandwidth requires a low loss filter with a narrow bandwidth to avoid frequency pulling of the laser frequency towards the peaks in the gain curve.

A birefringent filter has the possibility of meeting the above requirements. The theory and applications of birefringent filters have been extensively covered in the literature [8]-[14]. In order to provide unambiguous continuous frequency tuning across the whole gain bandwidth of the Co:MgF_2 laser, without possible frequency jumps between various filter resonances, one should choose the optical axis of the birefringent plates to make an angle to the surface of the plates. This case has not been covered in detail in the literature.

In this paper an analysis of a multielement birefringent filter is presented which includes the case where the optical axis makes an angle to the plate surface. This analysis constitutes a major part of the paper. A three-element filter has been designed [15] which satisfies the requirements listed above for the Co:MgF_2 laser. The first high-frequency-resolution tuning characteristics of a *Q*-switched Co:MgF_2 laser are presented. This laser has been developed for atmospheric spectroscopy and remote sensing applications, which require that the laser linewidth be less than or equal to 3 GHz (0.1 cm^{-1}), corresponding to the pressure broadened linewidth at 1 atm of most target species of interest. This goal is achieved by insertion of an etalon into the laser cavity in addition to the birefringent filter.

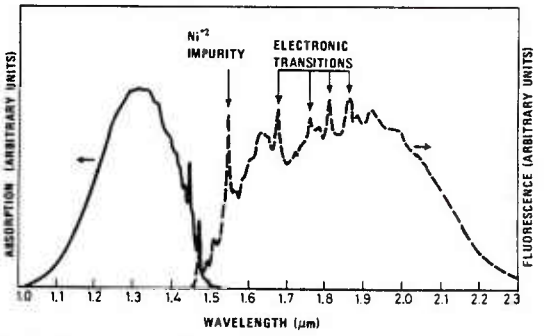

Fig. 1. Measured absorption and fluorescence spectrum for Co:MgF_2 between 1.0 and 2.3 μm.

II. Theory

A birefringent filter for laser frequency tuning consists of one or more birefringent plates oriented at Brewster's angle inside the laser resonator. The plates act both as retarding plates and polarizing elements. *p*-polarized light incident on the plates is transformed into elliptically polarized light inside the plates with continuously varying eccentricity of the ellipse as the beam propagates through the crystal. Certain wavelengths will be linearly *p*-polarized at the exit surface of the plates and will be transmitted with no Fresnel reflection losses. The filter is tuned by rotating the plates about the axis normal to the surface, thereby varying the effective principal refractive indexes of the plates.

The main reason for choosing the optical axis to make an angle to the plate surface is to increase the tuning rate versus plate rotation. This is important because of the narrowness of

Manuscript received July 9, 1984; revised November 12, 1984. This work was supported in part by the National Aeronautical and Space Administration, by the Air Force Engineering and Service Center, and by the Air Force Aerospace Medical Division. S. Løvold was also supported in part by the Norwegian Defence Research Establishment and by the Royal Norwegian Council for Industrial and Scientific Research.

S. Løvold was with the Lincoln Laboratory, Massachusetts Institute of Technology, Lexington, MA 02173. He is now with the Norwegian Defence Research Establishment, N-2007, Kjeller, Norway.

P. F. Moulton, D. Killinger, and N. Menyuk are with the Lincoln Laboratory, Massachusetts Institute of Technology, Lexington, MA 02173.

0018-9197/85/0300-0202$01.00

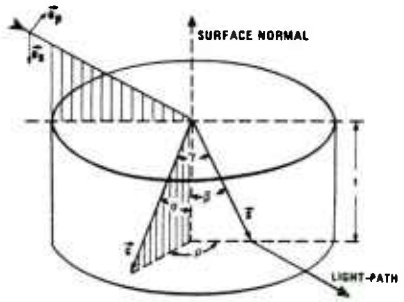

Fig. 2. A one-element birefringent filter. The plate is oriented at Brewster's angle to the incoming beam. β is the internal Brewster's angle and $\vec{s}$ is the direction of beam propagation in the plate. The *c*-axis is the optical axis of the plate. The unit vectors $\vec{e}_p$ and $\vec{e}_s$ are parallel to the *p*- and *s*-polarization of light incident on the plate. The plate is rotated an angle ρ defined in the figure. γ is the angle between the *c*-axis and the direction of beam propagation, and t is the thickness of the plate.

the plate rotation domains where the modulation depth of the filter is good.

In addition, one of these domains is broader when the optical axis points out of the surface, compared to when it lies in the plane of the plate. These effects will be shown in the following discussion.

A one-element birefringent filter is shown schematically in Fig. 2. The light is incident on the plate at Brewster's angle. (β is the internal Brewster's angle.) Using the Jones vector formalism (16), the electric field vector $\vec{E}$ is represented as

$$\vec{E} = E_p\vec{e}_p + E_s\vec{e}_s \tag{1}$$

where E_p and E_s are the *p*- and *s*-polarized electric field vector components along the unit vectors $\vec{e}_p$ and $\vec{e}_s$ respectively. The *c*-axis of the plate (the optical axis) makes an angle σ to the surface normal, and the plate is rotated an angle ρ as defined in the figure.

After transmission through the plate, the electric field components are given by

$$\begin{pmatrix} E_{p,\,\mathrm{out}} \\ E_{s,\,\mathrm{out}} \end{pmatrix} = I \cdot M \cdot I \begin{pmatrix} E_{p,\,\mathrm{in}} \\ E_{s,\,\mathrm{in}} \end{pmatrix} \tag{2}$$

where the matrix I describes the transmission through a plate interface and the matrix M describes the transmission through the birefringent material. ($\cdot$ means standard matrix multiplication.) I is given by (17)

$$I = \begin{pmatrix} 1 & 0 \\ 0 & q \end{pmatrix} \tag{3}$$

where $q = 2n/(n^2 + 1)$ is the transmittance of the *s*-polarized electric field at Brewster's angle into a medium with index of refraction n. The matrix M is given by [16], [11]

$$M = \begin{pmatrix} \cos^2\theta + \sin^2\theta e^{j\Delta\phi} & \cos\theta \sin\theta(e^{j\Delta\phi} - 1) \\ \cos\theta \sin\theta(e^{j\Delta\phi} - 1) & \sin^2\theta + \cos^2\theta e^{j\Delta\phi} \end{pmatrix}. \tag{4}$$

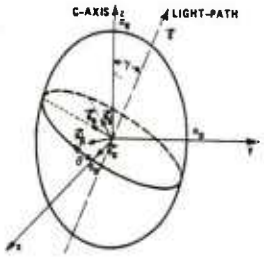

Fig. 3. The index ellipsoid of a positive uniaxial birefringent crystal [17]. The vector $\vec{s}$ is parallel to the direction of the beam propagation in the crystal, which makes an angle γ to the optical axis (the *c*-axis). The orthogonal unit vectors $\vec{e}_p$ and $\vec{e}_s$ are parallel to the *p*- and *s*-polarization of the electric field, inside the plate. The orthogonal unit vectors $\vec{e}_o$ and $\vec{e}_e$ are parallel to the semiminor and semimajor axis, respectively, of the ellipse defined by the intersection of the $\vec{s}$-plane with the ellipsoid. θ is the angle between $\vec{e}_p$ and $\vec{e}_o$.

Here θ is the angle between the unit vectors $\vec{e}_o$ and $\vec{e}_p'$. The vector $\vec{e}_o$ is parallel to the direction in the plate where the index of refraction is n_o, and $\vec{e}_p'$ and $\vec{e}_s'$ are the unit vectors parallel to the *p*- and *s*-polarization for the electric field inside the plate, as shown in Figs. 2 and 3. (The matrix M is obtained by simply transforming the electric field from the coordinate system e_p', e_s' to $\vec{e}_o$, $\vec{e}_e$ (see Fig. 3), and back again to $\vec{e}_p'$, $\vec{e}_s'$ after propagation through the crystal.) $\Delta\phi$ is the phase retardation of the plate, and is given to a good approximation when $n_e - n_o \ll n_o$ by [17]

$$\Delta\phi = \frac{2\pi}{\lambda}\frac{t}{\cos\beta}(n_e - n_o)\sin^2\gamma. \tag{5}$$

Here t is the thickness of the plate, n_o and n_e are the ordinary and extraordinary indexes of refraction respectively, and γ is the angle between the *c*-axis and the direction of the beam propagation $\vec{s}$ in the crystal. The wavelengths for which $\Delta\phi = N2\pi$, where N is an integer, will have the same polarization at the exit interface as at the entrance interface of the plate.

The angles γ and θ entering (4) and (5) can be expressed by the angles ρ, β, and σ (Fig. 2) through the equations

$$\cos\gamma = \cos\beta\cos\sigma + \sin\beta\sin\sigma\cos\rho \tag{6}$$

$$\cos\theta = \sin\rho\sin\beta/\sin\gamma. \tag{7}$$

(Eqs. (6) and (7) can be obtained from the vector multiplications $\vec{c}\cdot\vec{s} = |c|\cdot|s|\cos\gamma$ and $\vec{e}_p'\cdot\vec{s}\times\vec{c} = |s|\cdot|c|\sin\gamma\cos\theta$, as can be seen from Figs. 2 and 3.)

With the possible addition of an equation describing the dispersion of the birefringent material, (1)–(7) form the basis for designing a tuning filter for a given laser. For crystal quartz, the dispersion equation

$$n_e - n_o = [8.5 - 0.65(\lambda - 1.5)] \times 10^{-3} \tag{8}$$

is a good approximation to experimental data for wavelengths λ (in micrometers) between 0.6 and 2.4 μm [18].

In designing a filter for a given wavelength region, care should be taken that the resonance condition, $\Delta\phi = N2\pi$, does not occur for plate rotation angles where the electric field polarization is parallel to the ordinary or extraordinary axis of

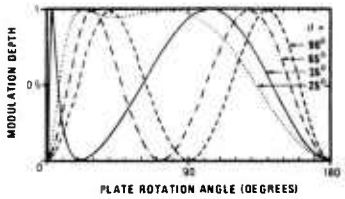

Fig. 4. The modulation depth, defined by (9), versus plate rotation angle ρ for various c-axis orientations. σ is the angle between the c-axis and the plate normal (see Fig. 2).

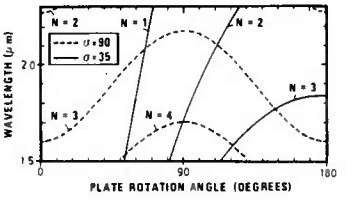

Fig. 5. Resonance wavelengths, for which the transmission for incident p-polarized light is 100 percent, versus plate rotation angle, for two different single-element filters. One filter is a 0.65 mm thick plate with angle $\sigma = 35°$ between the optical axis and the plate normal. The resonances are indicated by solid lines. The other filter is a 0.68 mm thick plate with $\sigma = 90°$, i.e., the optical axis is in the plane of the plate. The resonances are indicated by the dashed curves. Both plates are of single crystal quartz.

the crystal. In these cases all wavelengths will be transmitted with no Fresnel reflection losses. This corresponds to the situation where the angle θ (Fig. 3) is 0 or 90°. It is useful to define the "modulation depth" MD by

$$\mathrm{MD} = |m_{21}(\max)|^2 = 4\cos^2\theta\sin^2\theta \tag{9}$$

where m_{21} is the off-diagonal element of the matrix M ($m_{21} = m_{12}$). Fig. 4 shows the modulation depth versus plate rotation angle for various c-axis orientations. The domains where MD is large defines the useful plate rotation angle domains. A design criterion for the filter is thus that only one filter resonance falls within such a domain and that this resonance covers the whole gain bandwidth of the laser in that domain.

Fig. 5 shows the resonance wavelengths for two different plates. One is a 0.65 mm thick crystal quartz plate with an angle $\sigma = 35°$ between the c-axis and the surface normal. The other is 0.68 mm thick of the same material with $\sigma = 90°$, i.e., the c-axis lies in the plane of the plate. It is clearly seen that the plate with $\sigma = 35°$ can be useful for tuning a Co:MgF_2 laser from 1.5 to 2.3 μm on the $N = 2$ resonance. This resonance falls within a domain where the modulation depth is large, as seen in Fig. 4. At the longer wavelengths the interference from the resonance $N = 3$ can cause a problem. However, the laser mirrors cannot easily be made to cover the whole spectral range from 1.5 to 2.3 μm with uniform reflectivity. Thus this possible interference should not cause any problems. If there should be an interference problem between the $N = 2$ and $N = 3$ resonances, one could use an additional plate with half the thickness, i.e., $t = 0.325$ mm. This plate would have its $N = 1$ resonance overlapping the $N = 2$ resonance of the 0.65 mm plate, and would have large losses at the $N = 1$ and $N = 3$ resonances of the 0.65 mm plate.

It can be seen in Fig. 4 that when the optical axis lies in the plane of the plate, i.e., $\sigma = 90°$, a single resonance order is limited to the spectral region from 1.6 to 2.15 μm when the plate is rotated from 0 to 90°. In addition, it was shown in Fig. 4 that the modulation depth is poor close to 0 and 90°. This is therefore not a good solution. It should be noted that one could choose a thicker plate and use two or more resonance orders to cover the gain bandwidth of the Co:MgF_2 laser. This would require a set of mirrors with center frequencies and bandwidths that were matched to such a filter. In this work, however, the filter with $\sigma = 35°$ has been found to be a better solution.

The transmission bandwidth of the filter (for a fixed rotation angle) determines the degree of laser frequency pulling towards peaks in the gain curve, and also determines the laser emission linewidth.

The transmission T of a birefringent filter can be defined as

$$T = \left|\frac{E_{p,\mathrm{out}}}{E_{p,\mathrm{in}}}\right|^2 \tag{10}$$

that is, the fraction of the incident p-polarization intensity that is left in the p-polarization after propagation through the filter. If the incident light is fully p-polarized and the birefringent plates were followed by a 100 percent p-polarizer, T would be the actual transmission of the filter. We assume that the transmission T as defined by (10) is useful for characterizing the transmission of a birefringent filter for a Co:MgF_2 laser because the modes with the highest net gain in such a laser will be linearly polarized. This is due to the birefringence of the MgF_2 crystal and usually the presence of several polarizing Brewster's angle interfaces in the resonator (i.e., the MgF_2 crystal interfaces, the Q-switch, and the vacuum-Dewar windows; see Section III).

The transmission bandwidth of a single plate filter operating on a low-order resonance will be broad, typically several hundred nanometers. Adding more plates with c-axes parallel to each other and thickness equal to a multiple of the thickness of the first plate will make the transmission bandwidth narrower, but will also introduce secondary transmission peaks. Fig. 6 shows the transmission T as defined by (9) for a three-element birefringent filter with c-axis angle $\sigma = 35°$ and thickness t, $2t$, and $10t$, where $t = 0.65$ mm. The plate rotation angle $\rho = 90°$. The peak transmission wavelength is at the second order resonance in the thinnest plate and at the 20th order resonance in the thickest plate.

In order to evaluate whether the laser wavelength will follow the main transmission peak of the filter, the transmission loss on the secondary peaks should be compared with the maximum difference in single-pass gain in the gain medium over corresponding wavelength intervals. For the filter shown in Fig. 6 the transmission losses are 15 percent at the secondary transmission peaks, at the 19th and 21st order resonance of the thickest plate. For the Co:MgF_2 laser the peak-to-valley gain ratio over a corresponding wavelength interval is 7/5 at around 1.7 μm, according to the fluorescence curve shown in

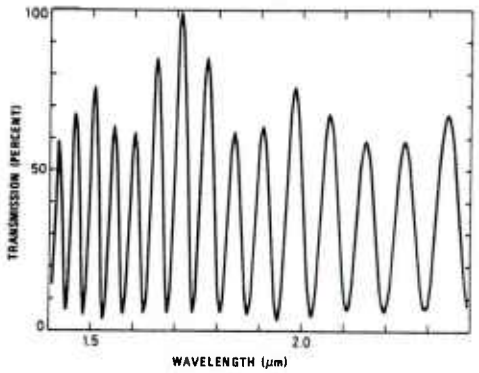

Fig. 6. The transmission T, as defined by (10), for a three-element crystal quartz birefringent filter. The c-axis angle $\sigma = 35°$. The c-axes are parallel to each other and the thicknesses of the plates are t, $2t$, and $10t$, where $t = 0.65$ mm. The plate rotation angle $\rho = 90°$.

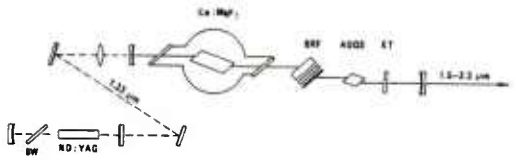

Fig. 7. The Co:MgF_2 laser system. The Co:MgF_2 crystal is mounted inside a liquid nitrogen Dewar. A three-element birefringent filter (BRF) and a quartz etalon (ET) are used for tuning of the Co:MgF_2 laser, and the laser has an acoustooptic Q-switch (AOQS). The Co:MgF_2 laser is pumped by a Nd:YAG laser with an internal Brewster window (BW), to force it to emit linearly polarized light.

Fig. 1. Assuming a laser resonator with an average 4.5 percent single-pass loss (for example 7 percent output coupling, 1 percent single-pass internal losses), one can calculate that the laser can be pumped 3 times above threshold for operation at a wavelength in the gain valley domain before the net laser gain can be positive at the peak gain wavelength. The laser can be pumped 8 times above threshold for operation in the gain valley domain before the net gain at the peak can exceed the net gain in the valley. The filter shown in Fig. 6 has more than 13 percent loss at the secondary transmission peaks across the whole gain bandwidth of the Co:MgF_2 laser. Thus since the Co:MgF_2 is such a low gain material and it is predominantly homogeneously broadened [4], this filter should have an adequate extinction ratio.

The laser emission linewidth is determined by the transmission bandwidth of the filter, the mode of operation of the laser, and whether the laser transition is homogeneously or inhomogeneously broadened. In Q-switched operation the linewidth will be determined by the filter transmittance raised to the power of $2N_{rt}$, where N_{rt} is the number of round trips a photon makes in the resonator during the build-up time of the laser pulse. In the Co:MgF_2 laser used in our experiments, $N_{rt} \approx 400$ when the laser is pumped 1.5 times above threshold, according to Q-switched laser theory [19], [20]. The transmittance of the filter shown in Fig. 6, raised to the power of $2N_{rt}$, will have a central peak width (FWHM) of 115 GHz (3.8 cm^{-1}) for $N_{rt} = 400$. Since the switching time for the acoustooptic Q-switch used in these experiments is relatively long (200–500 ns, corresponding to 40–100 round-trips) and since the laser transition is predominantly homogeneously broadened, the laser emission linewidth is expected to be narrower, but of the same order of magnitude, as the calculated 115 GHz, for pumping 1.5 times above threshold. This is in good agreement with the experimental results (see Section IV).

The number of round trips during the build-up time of the Q-switched laser pulse is roughly proportional to $\{T_0[(P/P_t) - 1]\}^{-1}$ where T_0 is the output coupling and P/P_t is the pumping relative to the threshold pump level [19], [20]. Since the "effective" transmission bandwidth of the filter is inversely proportional to the square root of the number of transmissions through the filter, it is expected that the laser linewidth will vary accordingly when the pump level or the output coupling are changed.

III. The Co:MgF_2 Laser

The Co:MgF_2 laser system is shown schematically in Fig. 7. The Brewster-angle-cut MgF_2 crystal is 27 × 6 × 6 mm in size and doped with 0.75 weight percent CoF_2. It is mounted inside a liquid nitrogen Dewar with Brewster windows and cooled to 77 K. The resonator mirror spacing is 70 cm and the mirror radii are 100 cm. The output mirror has 5 percent transmission, centered at 1.75 μm. The Co:MgF_2 laser is longitudinally pumped by a Nd:YAG laser, which emits 400 mJ, 800 μs duration linearly polarized multimode pulses at 1.32 μm. (Without the Brewster window inside the Nd:YAG laser resonator, the output energy is 500 mJ randomly polarized for the same input energy.) The pump pulses are focused using a 25 cm focal length lens to a 1 mm diameter spot in the Co:MgF_2 laser crystal, exciting only the TEM_{00} mode of the Co:MgF_2 laser resonator.

The laser frequency can be tuned by a three-element birefringent filter (BIFF or BRF) and a 1 mm thick uncoated quartz etalon. The BRF has been chosen with c-axis angle $\sigma = 35°$ and thickness t, $2t$, and $10t$ where $t = 0.65$ mm, as described in the preceeding section. Alignment of the individual plates with their c-axis parallel to each other was first done external to the laser using a He–Ne laser and calculated rotation angles for resonances at 0.6328 μm. The filter was then mounted inside the Co:MgF_2 laser and the individual plates were fine-adjusted for maximum laser output. From measurements of the threshold for laser oscillation before and after insertion of the filter, the single-pass insertion loss was calculated to be less than 1 percent.

The laser was Q-switched by a Brewster-angle-cut fused silica acoustooptic Q-switch. The single-pass insertion loss of the Q-switch was measured to be less than 0.5 percent.

IV. Results

The temporal and spectral characteristics of the laser output have been measured. The spectral characteristics were measured with a 1 m grating spectrometer with 3 GHz (0.1 cm^{-1}) resolution, and with a plane-parallel scanning Fabry–Perot interferometer. The system finesse of the Fabry–Perot interferometer has been measured to be better than 20. The laser

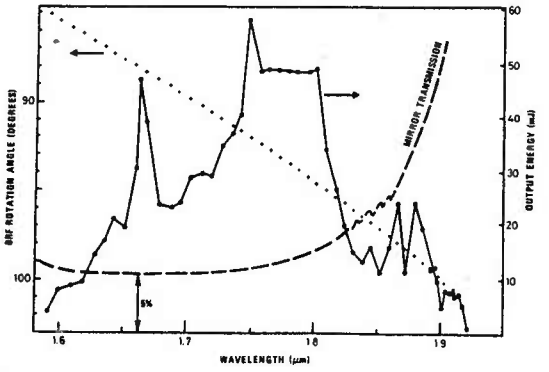

Fig. 8. The measured laser output wavelength versus birefringent filter rotation, and the measured output pulse energy versus wavelength. The laser was operated in a free-running (gain-switched) mode without the Q-switch and the etalon. The transmission losses of the laser mirrors are also shown.

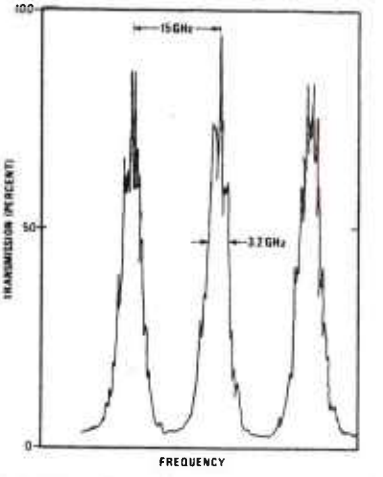

Fig. 9. Fabry-Perot interferometer scan of the laser beam, for a fixed laser frequency. The free spectral range of the interferometer is 15 GHz (1 cm mirror separation). The laser PRF is 3 Hz and the laser pulses are sampled by a boxcar signal averager. The interferometer scan rate is 12 GHz/min.

frequency has also been scanned across an absorption line of HCl.

Fig. 8 shows the measured laser output wavelength versus BRF rotation, and the measured output pulse energy versus wavelength. In this case the Q-switch and the etalon were removed. The laser was pumped with approximately 400 mJ at a 3 Hz pulse repetition rate. It can be seen that the laser wavelength tunes smoothly with the BRF rotation, and there is an excellent agreement between the measured tuning characteristics and those calculated for $N = 2$, as shown in Fig. 5. No frequency pulling towards the peaks in the gain curve could be observed to within the measurement accuracy of the grating spectrometer. The same smooth tuning characteristics were obtained during Q-switched operation.

With the present set of resonator mirrors, the laser could be tuned from 1.6 to 1.9 μm. At wavelengths longer than 1.8 μm the combined effect of mirror loss and strong absorption from water-vapor in the air limits the output energy and tuning range. The total transmission of the two resonator mirrors is shown in Fig. 8. (The water-vapor absorption can of course be avoided by placing the whole resonator in vacuum or in a dry nitrogen atmosphere. This has not been done in these experiments.) The two strong peaks in the output energy at 1.67 and 1.75 μm correspond to electronic transitions in the gain spectrum, as seen in Fig. 1.

The temporal and spectral characteristics of the laser output were measured during Q-switched operation. The laser was pumped approximately 1.5 times above threshold at various wavelengths between 1.67 and 1.8 μm. The measured output pulse energy and pulse duration was ~15 mJ and 600 ns respectively, in good agreement with Q-switched laser theory [19], [20].

In Q-switched operation and without an etalon in the cavity the laser emission linewidth was measured to be ~100 GHz (~3 cm^{-1}). This is in good agreement with what could be expected from the transmittance characteristics of the BRF, as discussed in Section II.

When the 1 mm thick uncoated quartz etalon was inserted into the cavity, the laser emission linewidth as measured with the scanning Fabry-Perot interferometer was found to be 3 GHz (0.1 cm^{-1}). Fig. 9 shows an interferometer scan with a 15 GHz free spectral range (1 cm mirror separation) for a fixed laser frequency. The frequency scan is very slow, so the spectrum is an average taken over many laser pulses. Apparently the laser oscillates on several longitudinal modes simultaneously. The pulse-to-pulse frequency variation and the frequency spectrum of a single pulse have not been measured.

The measured 3 GHz laser emission linewidth is close to the value expected on the basis of the transmission characteristics of the etalon. Assuming 400 round-trips in the resonator during the build-up time for the laser pulse for pumping 1.5 times above threshold, the bandwidth of the etalon transmission lobes will be 5 GHz (FWHM) (see Section II).

A laser frequency scan requires a simultaneous tuning of the birefringent filter and the etalon. The laser may be tuned across a 10 GHz frequency range (the free spectral range of the etalon) by tilting the etalon and keeping the BRF fixed. Fig. 10 shows such a scan across the first overtone of the R3 line of HCl^{37}, at $\lambda = 1.7436$ μm [21]. The absorption cell contained 50 torr of HCl and 700 torr of air. The measured linewidth is approximately 5 GHz which agrees well with the expected pressure broadened linewidth at 1 atm pressure. During the scan shown in Fig. 10 the laser was operated in a free-running (gain switched) mode, in which case the laser linewidth has been measured to be less than 1.2 GHz (0.04 cm^{-1}).

V. Discussion and Conclusion

In order to keep the output energy level well below the threshold for laser mirror damage [6], the laser was pumped only 1.5 times above threshold in these experiments. A lidar system has been built, using this laser as a transmitter, which has demonstrated path-averaged absorption spectroscopy of

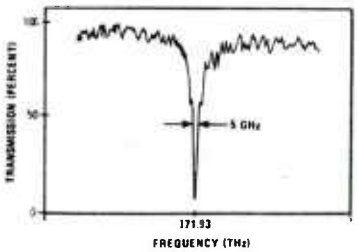

Fig. 10. A laser-frequency scan across the first overtone of the R3 line of HCl^{37}, at 171.9 THz (λ = 1.7436 μm). The laser was operated in a free-running (gain-switched) mode. The absorption cell contained 50 torr of HCl and 700 torr of air.

atmospheric species with 3 GHz spectral resolution out to 7.35 km [22]. Separate experiments have demonstrated that by using a higher output coupling, at least 60 mJ output pulses with 150 ns duration can be extracted from the Co:MgF_2 laser at 1.96 μm without damage to the laser mirrors or the crystal. This should allow range-resolved atmospheric remote sensing measurements to be made with 25 m spatial resolution out to several kilometers [23], [24].

It should be noted that when the laser is pumped further above threshold or when the output coupling is increased, the build-up time for the *Q*-switched laser pulse is decreased. This is expected to give a broader laser emission linewidth, as discussed in Section II. It may thus then be necessary to use a sharper filter than the 1 mm thick uncoated quartz etalon in order to obtain a 3 GHz or smaller laser emission linewidth. As an alternative, the loss of the *Q*-switch can be adjusted to allow the laser to operate slightly above threshold during the initial stage of the pump pulse, thus allowing formation of a narrow-line width signal in the cavity. The *Q*-switch loss can then be reduced to zero to generate a short, energetic pulse.

In conclusion, a tunable *Q*-switched Co:MgF_2 laser system has been developed which has demonstrated that the Co:MgF_2 laser has good temporal and spectral characteristics which are suitable for atmospheric spectroscopy and remote sensing applications.

Acknowledgment

The authors would like to extend their appreciation to A. Mooradian and P. Kelley for their encouragement and for numerous valuable discussions. They would also like to acknowledge the expert technical assistance of W. E. DeFeo and E. F. Casazza. The first author would like to express his gratitude to A. Mooradian and P. Kelley and his colleagues at Lincoln Laboratory for an inspiring and pleasant sabbatical year at the laboratory.

References

[1] L. F. Johnson, R. E. Dietz, and H. J. Guggenheim, "Optical maser oscillation from Ni^{2+} in MgF_2 involving simultaneous emission of phonons," *Phys. Rev. Lett.*, vol. 11, pp. 318–320, 1963.
[2] P. F. Moulton, A. Mooradian, and T. B. Reed, "Efficient CW optically pumped Ni:MgF_2 laser," *Opt. Lett.*, vol. 3, pp. 164–166, 1978.
[3] P. F. Moulton and A. Mooradian, "Broadly tunable CW operation of Ni:MgF_2 and Co:MgF_2 lasers," *Appl. Phys. Lett.*, vol. 35, pp. 838–840, 1979.
[4] P. F. Moulton and A. Mooradian, "Tunable transition-metal doped solid state lasers," in *Laser Spectroscopy IV*, H. Walther and K. W. Rothe, Eds. Berlin, West Germany: Springer-Verlag, 1979, pp. 584–589.
[5] Lincoln Laboratory, M.I.T., Solid State Res. Rep. DTIC ADA-094075, pp. 11–13, 1980.
[6] P. F. Moulton, "Pulse-pumped operation of divalent transition-metal lasers," *IEEE J. Quantum Electron.*, vol. QE-18, pp. 1185–1188, Aug. 1982.
[7] H. P. Jenssen, M.I.T. Cambridge, and P. F. Moulton, preliminary data, unpublished.
[8] B. Lyot, "Un monochromateur a grand champ utilisant les interferences en lumiere polarisee," *Compt. Rend.*, vol. 197, pp. 1593–1595, 1933.
[9] J. W. Evans, "The birefringent filter," *J. Opt. Soc. Amer.*, vol. 39, pp. 229–242, 1949.
[10] J. M. Yarborough and J. Hobart, presented at the 1973 IEEE/OSA Conf. Laser Eng., Appl., Washington, DC, May 30–June 1, 1973.
[11] A. L. Bloom, "Modes of a laser resonator containing tilted birefringent plates," *J. Opt. Soc. Amer.*, vol. 64, pp. 447–452, 1974.
[12] G. Holtom and O. Teschke, "Design of a birefringent filter for high-power dye-lasers," *IEEE J. Quantum Electron.*, vol. QE-10, pp. 577–579, 1974.
[13] D. R. Preuss and J. L. Gole, "Three-stage birefringent filter tuning smoothly over the visible region: Theoretical treatment and experimental design," *Appl. Opt.*, vol. 19, pp. 702–710, 1980.
[14] A. A. Kachanov, Birefringent selector of the emission wavelength for a CW dye laser," *Sov. J. Quantum Electron.*, vol. 12, pp. 927–929, 1982.
[15] Computer programs, written in BASIC on a DEC Minc computer with a VT-125 Graphic terminal, are available from the authors.
[16] R. C. Jones, "A new calculus for the treatment of optical systems," *J. Opt. Soc. Amer.*, vol. 31, pp. 488–503, 1941.
[17] M. Born and E. Wolf, *Principles of Optics*, 4th ed. New York: Pergamon, 1970, p. 699.
[18] W. L. Wolfe, "Properties of optical materials," in *Handbook of Optics*, W. G. Driscoll and W. Vaughan, Eds. New York: McGraw-Hill, 1978, pp. 7–82.
[19] W. G. Wagner and B. A. Lengyel, "Evolution of the giant pulse in a laser," *J. Appl. Phys.*, vol. 34, pp. 2040–2046, 1963.
[20] W. Koechner, "Solid-state laser engineering," in *Springer Series in Optical Sciences*, vol. 1. New York: Springer-Verlag, 1976, pp. 399–402.
[21] L. S. Rothman, "A.F.G.L. trace gas compilation," Air Force Geophys. Lab., Hanscom AFB, MA.
[22] D. Killinger, N. Menyuk, and S. Løvold, to be published.
[23] R. L. Byer, "Review, remote air pollution measurement," *Opt. Quantum Electron.*, vol. 7, pp. 147–177, 1975.
[24] D. J. Brassington, "Differential absorbtion lidar measurements of atmospheric water vapor using an optical parametric oscillator source," *Appl. Opt.*, vol. 21, pp. 4411–4416, 1982.

S. Løvold, photograph and biography not available at the time of publication.

P. F. Moulton, photograph and biography not available at the time of publication.

D. K. Killinger
He received the B.A. degree from the University of Iowa, Iowa City, IA, in 1967, the M.A. degree from DePauw University, Greencastle, IN, in 1969, and the Ph.D. degree in physics from the University of Michigan, Ann Arbor, MI, in 1978.

From 1968 to 1974, he conducted research on optical and microwave atmospheric propagation and radar analysis while employed as a research physicist at the Naval Avionics Facil-

ity. Between 1974 and 1978, he was a Research Assistant at the University of Michigan, where his research activities centered around laser physics, quantum optics, and molecular spectroscopy. He held a postdoctoral position at Ford Scientific Research Laboratory between 1978 and 1979 where his research included the UV spectroscopy and laser-induced saturation fluoresence of the OH free radical. In 1979, he joined the Research Staff of the Quantum Electronics Group at Lincoln Laboratory and is currently Program Manager of the Laser Remote Sensing Program. His present research activities have been directed toward the development of new laser sources and optical detection techniques for laser remote sensing applications.

Dr. Killinger is a member of the American Physical Society and a Fellow of the Optical Society of America.

N. Menyuk, photograph and biography not available at the time of publication.

0018-9197/85/0300-0208$09.00

APPENDIX C

The following is a reprint of a journal article published in Science, 2 January 1987, entitled "Laser Remote Sensing of the Atmosphere."

Reprint Series
2 January 1987, Volume 235, pp. 37–45

SCIENCE

Laser Remote Sensing of the Atmosphere

DENNIS K. KILLINGER AND NORMAN MENYUK

Laser Remote Sensing of the Atmosphere

DENNIS K. KILLINGER AND NORMAN MENYUK

Laser beams can be used as long-range spectroscopic probes of the chemical composition and physical state of the atmosphere. The spectroscopic, optical, and laser requirements for atmospheric laser remote sensing are reviewed, and the sensitivity and limitations of the technique are described. A sampling of recent measurements includes the detection of urban air pollution and toxic chemicals in the atmosphere, the measurement of global circulation of volcanic ash in the upper atmosphere, and the observation of wind shear near airports.

LASER REMOTE SENSING OF ATMOSPHERIC PROPERTIES from a single location is referred to as lidar, an acronym for light detection and ranging, and is analogous to radar (*1–6*). In lidar, the projection of a short laser pulse is followed by reception of a portion of the radiation reflected from a distant target or from atmospheric constituents such as molecules, aerosols, clouds, or dust (Fig. 1). The incident laser radiation interacts with these constituents, causing alterations in the intensity and wavelength according to the strength of this optical interaction and the concentration of the interacting species in the atmosphere. Consequently, information on the composition and physical state of the atmosphere can be deduced from the lidar data. In addition, the range to the interacting species can be determined from the temporal delay of the backscattered radiation. Lidar has been used to measure the movement and concentration of air pollution near urban centers, the chemical emission around industrial plants, and atmospheric trace chemicals in the stratosphere. Lidar has also been used to measure the velocity and direction of winds near storms and airports and to track the global circulation of volcanic ash emitted into the atmosphere after recent eruptions, such as those at Mount St. Helens and El Chichón. Under optimal conditions lidar can be extremely sensitive. An example is the ground-based laser remote sensing of sodium and lithium atoms in the stratosphere at ranges greater than 90 km and in concentrations as low as a few atoms per cubic centimeter (*5*). More commonly, detection ranges are on the order of a few hundred meters to several kilometers and concentration levels on the order of parts per million to parts per billion.

The use of optical backscatter to measure properties of the atmosphere is not new, extensive experiments having been conducted in the early 1900's with large searchlights. The field of optical remote sensing was greatly advanced by the laser, which offers several improvements over conventional light sources. These include narrow spectral width (<0.01 nm), a frequency or color that is often tunable, and high peak power (>10^6 W) available in a short pulse (<1 μsec) and in a narrow beam (<10 cm in diameter). These attributes make the laser an ideal spectroscopic probe of the atmosphere. In this regard, a lidar system may be thought of as an "active" remote sensing system since it can illuminate the target region, in contrast to a "passive" optical sensor which detects ambient light or thermal emission from the target.

The applications of lidar systems for the remote sensing of atmospheric properties were appreciated soon after the discovery of lasers in the early 1960's. Early lidar measurements were made in 1962 by Fiocco and Smullin (*7*) who bounced a laser beam off the moon and who also investigated the turbid layers in the upper atmosphere; in 1963 by Ligda (*8*) who used a ruby laser to obtain the first lidar measurements of cloud heights and tropospheric aerosols; and in 1964 by Schotland (*9*) who used a temperature-tuned ruby laser to detect water vapor in the atmosphere. Progress has been continuous since that time, but the discovery of different laser sources in the past decade, coupled to improvements in optical instrumentation and data processing, has been responsible for the recent surge in the number of laser remote sensing systems. This improved capability has been accompanied by an increased awareness of the need to monitor the impact of natural and anthropogenic influences on the environment.

Remote sensing of the atmosphere by optical techniques can be accomplished in several ways. One technique involves measurement of the absorption spectrum of the atmosphere over a long path separating a spectroscopic optical source and a detector (*5*). Another long-path absorption technique uses a configuration, described by Hinkley and Kelley (*10*), in which a tunable laser source and detector are located together and a retroreflecting mirror is placed at a distance of several hundred meters; such a system is useful when the laser source is weak, since the retroreflector greatly enhances the returned radiation. In this article we will primarily be concerned with a pulsed lidar system where the laser and detector are located together and no retroreflector is used as the target; in this case the returned laser radiation is due to backscatter from aerosols or dust in the atmosphere or a topographic target such as a hill or trees.

The authors are at the Massachusetts Institute of Technology, Lincoln Laboratory, Lexington, MA 02173-0073.

Optical Requirements for Laser Remote Sensing

The physics and optical technology associated with atmospheric laser remote sensing encompass atmospheric optical propagation, atomic and molecular spectroscopy, digital signal processing, and laser technology. In this section we discuss the optical requirements for lidar and, in particular, review (i) the presence of transmission "windows" in the atmosphere which permit the laser beam to propagate through the atmosphere with little attenuation, (ii) the identification and relative strength of the various optical interactions between an atmospheric species and a laser beam, and (iii) the properties of suitable lasers.

Atmospheric transmission windows. For a laser beam to detect a species at a long distance, the beam must not be appreciably attenuated by the intervening atmosphere. The output wavelength of the laser must therefore lie in a spectral transmission "window" of the atmosphere. These windows are shown as clear areas in Fig. 2, which shows a low-resolution transmission spectrum of the atmosphere over the spectral region from the ultraviolet to the mid-infrared (15 μm) for a path of 300 m (*11*). The atmosphere has regions of strong absorption as well as transmission windows; the absorption regions are due primarily to oxygen, carbon dioxide, and water vapor, and exhibit finer detail than that shown in the figure. The most useful transparent spectral ranges of the atmosphere are the visible (0.4 to 0.7 μm), near infrared (0.7 to 1.5 μm), and 3- to 5-μm and 9- to 13-μm regions. Within these spectral regions, the laser is not appreciably attenuated except by clouds, and thus remote sensing over long distances may be achieved.

Optical interaction of lasers with atmospheric species. The primary influence of the atmosphere on a low-power laser beam is through scattering and absorption. Both processes cause an attenuation of the beam according to Bouguer's or Beer's law

$$I = I_0 e^{-\alpha R} \quad (1)$$

where I is the intensity of the optical beam after transmission over a distance R, α is the atmospheric extinction coefficient, and I_0 is the initial intensity of the beam. It is possible to express α as a sum of terms

$$\alpha = \alpha_{Ray} + \alpha_{Mie} + \alpha_{Raman} + \alpha_{abs} \quad (2)$$

where α_{Ray}, α_{Mie}, and α_{Raman} are the extinction coefficients related to Rayleigh, Mie, and Raman scattering, respectively, and α_{abs} is the molecular absorption coefficient (*3*). Rayleigh scattering is due to particles in the atmosphere, such as molecules or fine dust, that are much smaller than the optical wavelength, λ, of the laser. Mie scattering is associated with larger particles such as aerosols whose size is on the order of λ. Rayleigh and Mie processes are elastic scattering: the scattered light is the same wavelength (color) as the incident laser beam. Raman scattering is an inelastic interaction of the optical beam involving excitation of the energy levels of a molecule and reradiation at a different wavelength. Absorption of the laser beam is a resonant interaction (direct absorption) leading to excitation of the molecule, followed possibly by fluorescence.

The sensitivity of laser remote sensing is related to the relative strength of these optical processes through the "lidar equation." The lidar equation (*2, 3*) is used to predict the power of the backscattered signal, P_r, and may be given in the form

$$P_r = \frac{P_t \rho A K e^{-2\alpha R}}{\pi R^2} \quad (3)$$

where P_t is the transmitted laser power, R is the range to the target, ρ is the effective reflectivity of the target (assumed to be larger than the laser beam), which backscatters the radiation into π steradians,

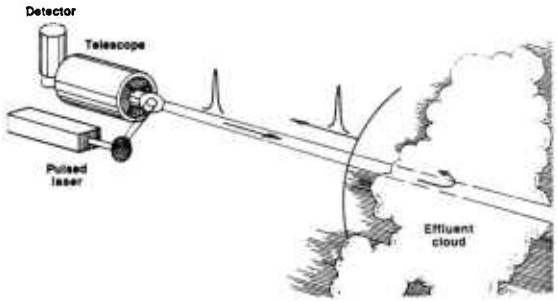

Fig. 1. Schematic of a lidar used for laser remote sensing of the atmosphere. The backscattered laser radiation may contain spectral information on the composition and physical condition of the cloud or the intervening atmosphere.

A is the area of the telescope, K is the optical efficiency of the system, and $\exp(-2\alpha R)$ is the two-way atmospheric attenuation of the optical beam. The more general form of Eq. 3 contains integrals over range, time, and spectral wavelength (*6*). The target can be either a solid reflector, such as a building or trees, or a "distributed" reflector consisting of molecules, dust, or clouds in the atmosphere. In the latter case, the target reflectivity term, ρ, is due to Mie, Rayleigh, Raman, or fluorescence processes and is thus also related to the associated α values.

The approximate strength of these processes is given in Table 1, which lists typical maximum values of ρ and α for some of the most important optical interactions (*3, 6*). The contribution of the scattering processes to both α and ρ arises because scattering reduces the intensity of the laser beam, contributing to extinction, whereas the portion of the beam that is scattered by 180° contributes to the detected signal, thereby serving effectively as a reflector. Absorption contributes only to the extinction coefficient, with no intrinsic contribution to ρ. In Table 1, values are given for ρ in conjunction with absorption, and refer to effective reflectivities arising from

Table 1. Optical interactions for laser remote sensing of the atmosphere; N.A., not applicable.

Optical interaction	Spectral range (μm)	Scatterer	Attenuation* α (km^{-1})	Effective† reflectivity ρ
Absorption (resonant)	UV	Atoms, molecules	10^{7}	10^{-2}
	1		10^{6}	10^{-3} to 10^{-1}
	10		10^{5}	10^{-7} to 10^{-4}
Scattering (non-resonant)				
Rayleigh	UV	O_2, N_2	10^{-1}	10^{-3}
	1		10^{-3}	10^{-5}
	10		10^{-7}	10^{-9}
Mie	UV	Aerosols, fine dust	10^{-1}	10^{-3}
	1		10^{-1}	10^{-4}
	10		10^{-2}	10^{-5}
Raman	UV	Molecules	10^{-5}	10^{-7}
	1		10^{-7}	10^{-9}
	10		10^{-11}	10^{-13}
Backscatter by hard targets	UV–1R	Buildings, trees, dense clouds	N.A.	10^{-2} to 1

*Attenuation calculated for concentration of 1 atm. †Reflectivity calculated for range resolution of 100 m, 1 atm concentration, and isotropic scattering.

fluorescence emission of the atom or molecule after it has absorbed the incident light (*12*). Conversely, a topographic target does not contribute to signal extinction; instead, the 180° scattered portion of the incident beam corresponds to the effective target reflectivity.

In general, the value of ρ or α may be a complicated function of laser linewidth, wavelength, or spectral filtering in the detection process, and may exhibit strong resonances. The values presented in Table 1 are appropriate to the strong resonance case and are appropriate only if the laser spectral requirements are met. The large values for α shown for absorption are for the case where the laser wavelength is coincident with an absorption line of the molecule; off-resonant values of α are orders of magnitude smaller. The backscatter and absorption coefficients, in general, depend on species concentration, temperature, pressure, and possibly velocity, so that lidar can measure one or more of these parameters. Measurements for all lidar systems are based on changes in the returned signal, P_r, as a function of wavelength or range, and thus deduce information about the physical state of the atmosphere through the effect of α or ρ.

A wide range of values occur for α and ρ (Table 1). Since all optical processes shown can occur simultaneously, it is important to design the lidar system, through judicious choice of laser wavelength, spectral filtering, or geometry, so that the measurement is most sensitive to only one optical interaction. In some lidar designs, α and ρ depend on different optical interactions; in other words, the attenuation and backscatter arise from different processes.

Lidar systems that measure a particular optical interaction have been classified as follows: (i) atmospheric backscatter lidar, (ii) differential-absorption lidar (DIAL), (iii) fluorescence lidar, (iv) Raman lidar, and (v) Doppler lidar. These classifications refer to the optical interaction to which the system has been designed to be most sensitive. Atmospheric backscatter lidar transmits one laser wavelength and detects changes in the backscatter due to the aerosols or dust in the atmosphere. DIAL measures the concentration of a molecular species in the atmosphere by transmitting two wavelengths, only one of which is absorbed, and detecting the difference in the intensity of the returns at the two wavelengths; the backscatter in DIAL may be from a hard target, or aerosol and dust returns as in atmospheric backscatter lidar. Fluorescence lidar uses two wavelengths as in a DIAL system and in addition uses spectrometric techniques to separate the wavelength-shifted fluorescence signal from the strong Rayleigh backscatter in the atmosphere. Raman and Doppler lidar uses a single-wavelength laser and sophisticated spectrometric detection techniques to spectrally resolve the wavelength-shifted signal from the strong background due to Rayleigh or Mie scattering. A Raman measurement often detects a wide spectral range (~10 nm) containing a number of vibrational-rotational Raman-shifted lines, whereas a Doppler measurement detects only a very narrow spectral range ($\sim 10^{-5}$ nm) that encompasses the Doppler-shifted backscatter lidar return. Because DIAL, fluorescence, and Raman techniques use several wavelengths that are either transmitted by the laser or detected by the lidar system, they provide measurements of the absolute concentration of the detected species. In contrast, atmospheric backscatter lidar uses a single-wavelength laser and single-wavelength detection and is best suited for lidar measurements that determine relative changes in the density of a known atmospheric species; these relative density measurements may, however, be referenced to an absolute value if the lidar is calibrated with the use of a standard target.

Laser sources. The utility of laser remote sensing is dependent on several factors, including the availability of lasers with sufficient output power and wavelength characteristics to provide an adequate lidar signal. Although many lasers provide high power, they often

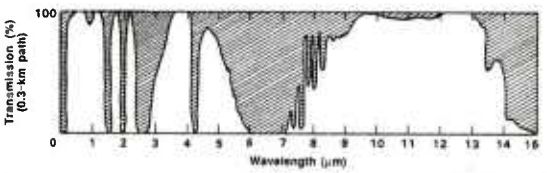

Fig. 2. Optical transmission of the atmosphere depicting the presence of strong absorption bands and transmission "windows" in the atmosphere.

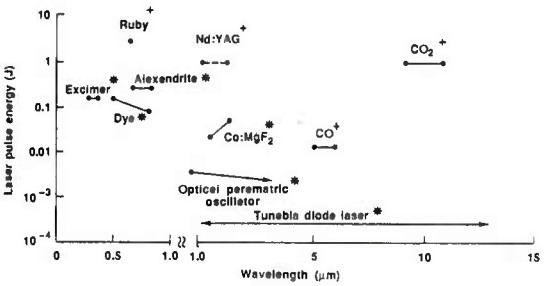

Fig. 3. Typical values of laser pulse energy as a function of laser wavelength tuning range showing the gaps in wavelength coverage of currently available lasers; (+) line tunable; (*) continuously tunable.

lack spectral coverage or tunability, preventing a determination of the resonant values of α or ρ (Table 1) for the particular atmospheric species or for the optical parameter of interest.

This may be better understood on the basis of Fig. 3, which presents the output energy per pulse now available from commercially available pulsed lasers of moderate size as a function of their wavelength coverage (*13, 14*). The wavelength tuning range of high-power lasers is not complete across the spectral range shown and is particularly lacking in the "eye-safe" spectral region ($\lambda > 1.4$ μm). For remote sensing in the infrared (IR), a minimum transmitted laser pulse energy on the order of 1 to 10 mJ is required for the detection of lidar signals from a hard target at a range of a few kilometers, and about 1 J for range-resolved returns from atmospheric aerosols. These values may be be lowered by one to two orders of magnitude if heterodyne detection can be used to detect the IR lidar return or if the remote sensing can be conducted in the visible or ultraviolet (UV). The detection of lidar atmospheric backscatter is much more sensitive in the latter spectral regions because detectors less susceptible to noise (such as photomultiplier tubes) are available and the atmospheric backscatter is improved in the UV-visible as compared to the IR.

The characteristics shown in Fig. 3 demonstrate why most laser remote sensing experiments have used ruby, dye, neodymium: yttrium-aluminum-garnet (Nd:YAG), and CO_2 lasers. These lasers offer sufficient energy for the detection of atmospheric species at moderate ranges, operate at wavelengths that are not appreciably attenuated by the atmosphere, and occur in a spectral range where several atmospheric constituents have reasonably strong optical interactions. Some of the lasers shown, such as Nd:YAG, CO, and CO_2, are line tunable in that they operate only on a limited number of discrete lines or wavelengths. The other lasers are continuously tunable within the spectral range shown in Fig. 3. Single-wavelength lasers are suitable for atmospheric backscatter, Raman, and Doppler lidar measurements since the spectral information is obtained during the detection process with a spectrometer or spectral filter. Lasers for DIAL or fluorescence lidar must be tunable, however, so that the laser wavelength can match the resonance

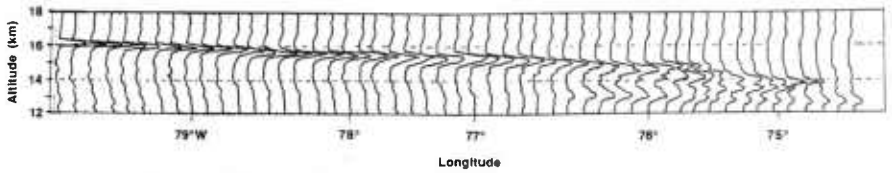

Fig. 4. Airborne lidar returns as a function of altitude and longitude near the coast of South Carolina on the evening of 27 May 1980 showing the increased lidar backscatter in a layer near 14 to 16 km due to volcanic material injected into the atmosphere by Mount St. Helens volcano. [Adapted from (*16*)]

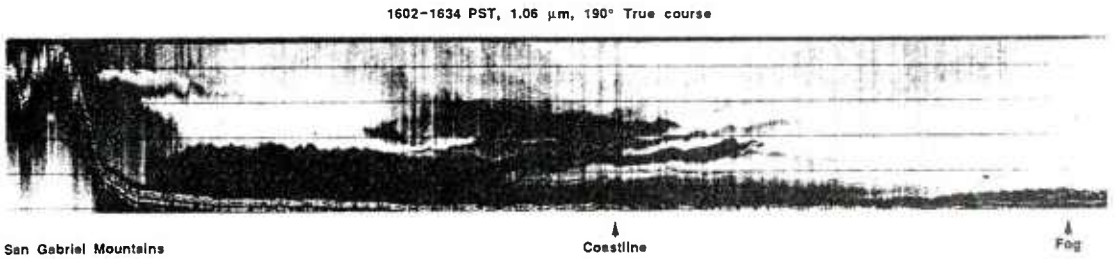

Fig. 5. Airborne lidar data near Los Angeles showing the vertical density profile of the boundary layer and continental flow of urban haze. [Adapted from (*17*)]

wavelength of the optical absorption lines of the molecules or atoms being detected. This is most important for the remote sensing of molecules or pollutants in the atmosphere because most of the absorption lines of many important organic species occur in the middle IR (2 to 5 μm) and this "fingerprint" spectral region does not coincide with many high-power, tunable laser sources. Because of these considerations, one of the most important goals in the future application of laser remote sensing is the development of new, high-power tunable lasers to cover the spectral gaps shown in Fig. 3.

Lidar Atmospheric Measurements

Each of the five lidar types can be used for the remote sensing of a selected variety of atmospheric constituents or parameters. Table 2 lists some of the constituents and parameters that have been measured with lidar. More detail is available in the technical digests of several recent lidar conferences (*15*).

Atmospheric backscatter lidar. Atmospheric backscatter lidar is the most common type of lidar system and consists of a nontunable, high-power, pulsed laser that is used to measure changes in the density or backscatter coefficient of the atmosphere that are due to particulates, such as aerosols, clouds, dust, or plumes. These atmospheric constituents have relatively large optical scattering cross sections and are relatively easy to detect (Table 1). Such lidars have been useful in tracking the turbid effluent and gas plumes from industrial smokestacks and have also been used to map out rain, snow, ice crystals, and dense clouds in the atmosphere (*1*). Precision measurements of the slight changes in the vertical density of the atmosphere have also been made with lidar, from which one can determine the pressure and temperature of the atmosphere as a function of altitude (*15*).

Recently, McCormick used a lidar system to track and map out the density of volcanic ash emitted into the atmosphere by Mount St. Helens and El Chichón (*16*). Figure 4 presents data obtained by McCormick using an airborne lidar system incorporating a high-power, frequency-doubled Nd:YAG laser operating near 0.53 μm (*16*). A thick layer of volcanic ash was detected at an altitude near 16 km and was found to vary in density and stratification as a function of distance. By tracking the cloud of volcanic ash, McCormick was able to use the ash as a tracer for global wind and circulation patterns. Such data, coupled with IR satellite data, showed the kinetics of global atmospheric circulation and tracked the slow global mixing of the volcanic ash between the Northern Hemisphere and the Southern Hemisphere that occurred the following year.

Atmospheric aerosols have also been studied by lidar in both the troposphere and the stratosphere. Lidar systems with beam-steering capabilities have been used by Uthe *et al.* for three-dimensional mapping of the flow of dense tropospheric aerosols (haze) near the ocean-land boundary and urban centers (*17*). An example of such measurements obtained near Los Angeles, showing the flow patterns of urban aerosols, is given in Fig. 5 (*17*). Such data have greatly increased our knowledge of the interplay of air circulation and pollution emission and are being used to predict the impact of emissions near urban centers.

Atmospheric backscatter lidar has been instrumental in investigations of the propagation of a laser beam through the atmosphere. These investigations have included the study of complicated scattering processes (*1*) present under normal atmospheric conditions due to the statistical distribution and variability of aerosols and scattering particles (*18*). In addition, the effect of multiple scattering has been investigated by lidar; multiple scattering is due to optically thick clouds that can drastically alter the transmission properties of a laser beam from that described by Eq. 1 (*19*).

Differential-absorption lidar. Most lidar measurements that determine the concentration of gaseous species in the atmosphere are presently made with the DIAL technique (*20*). This technique uses two or more wavelengths to measure the difference in the absorption of the lidar signal as the laser frequency is varied between a wavelength that is absorbed by molecules in the atmosphere and a wavelength that is not absorbed. The method is sensitive because it takes advantage of the relatively large value of the "on-resonance" absorption coefficient α (Table 1).

In principle, the concentration of an atmospheric species may be obtained directly from Eqs. 2 and 3 on the basis of measurements at a single wavelength. However, a concentration determination based on Eq. 3 and a single-wavelength measurement requires an accurate

knowledge of K, ρ, α, and the geometric factors R and A. In general, these parameters are either unknown or known with poor accuracy.

The DIAL technique attempts to overcome this problem by measuring the lidar signals at two wavelengths, λ and λ'. The laser wavelength λ is chosen to coincide with a wavelength strongly absorbed by the molecule being investigated, while at λ' there is little or no absorption. The use of two wavelengths results in two equations of the form of Eq. 3, which are then solved simultaneously for N_a, the path-averaged concentration of the absorbing molecule to yield

$$N_a = \frac{1}{2(\sigma_a' - \sigma_a)R}\left[\ln\left(\frac{P}{P'}\right) + \ln\left(\frac{\rho'}{\rho}\right) + 2(\alpha - \alpha')R\right] \quad (4)$$

where σ_a is the absorption cross section of the absorbing molecule, P is the backscattered signal power normalized to the transmitted power ($P = P_r/P_t$), and the primed and unprimed parameters refer to values at the low- and high-absorption wavelengths λ' and λ, respectively (*20*). In deriving Eq. 4 from Eq. 3, the $e^{-2\alpha R}$ term in Eq. 3 has been replaced by $e^{-2(\alpha + N_a\sigma_a)R}$, where α now represents the assumed known total attenuation of the atmosphere except that due to absorption, and $N_a\sigma_a$ is the attenuation due to absorption by the molecule being investigated.

The advantage of this two-frequency (DIAL) approach is that only differences in the various parameters need be considered. For this reason the DIAL technique is more commonly used for species concentration determination than single-frequency absorption measurements, despite the added complexity of a dual-frequency lidar system. Further simplification can be achieved when the use of closely spaced frequencies in a given measurement results in differences of target reflectivity ($\Delta\rho$) and atmospheric background extinction ($\Delta\alpha$) that are negligibly small. In that case, Eq. 4 reduces to

$$N_a = \frac{\ln(P_a/P_a')}{2(\sigma_a - \sigma_a')R} \quad (5)$$

The form given in Eq. 5, which greatly simplifies the relation between the lidar return ratio and species concentration, is frequently assumed in DIAL measurements, but Eq. 4 must be used in cases where either $\Delta\rho$ or $\Delta\alpha$ is nonnegligible. Equation 5 is valid for column-content or path-averaged DIAL measurements and is slightly changed for range-resolved measurements.

A large number of molecular species have been studied with the DIAL technique, and the results of many of these experiments are given in the proceedings of recent conferences (*15*), including extensive review articles on DIAL by T. Wilkerson and by E. Browell. The lidar systems used in these DIAL measurements span the frequency range from the UV to the IR and cover both range-resolved (RR) and path-averaged or column-content (CC) measurements.

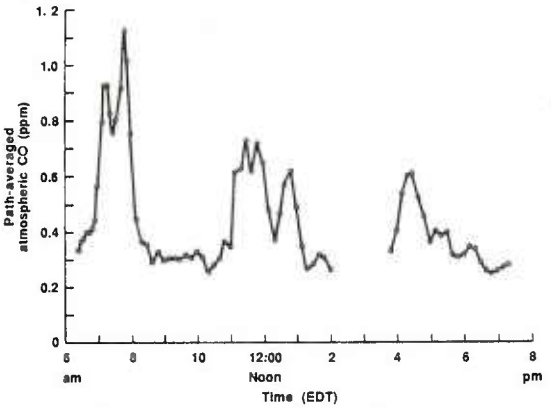

Fig. 6. CO_2 DIAL laser remote sensing of atmospheric CO for a path over a traffic roadway. Roadway range, 480 m; lidar range, 500 m.

Most DIAL experiments to date have used lidar signals backscattered from either a retroreflector or topographic targets (trees, buildings) to measure the column content of the atmospheric species between the laser transmitter and the target. Furthermore, mosr of these experiments have been carried out in the IR, where almost all molecules of interest have extensive absorption bands. The molecules investigated in CC DIAL experiments include SO_2, NH_3, O_3, CO, CO_2, HCl, H_2O, NO, N_2H_4, N_2O, and SF_6 (*4–6, 21*). The sensitivity of many of these CC DIAL measurements is on the order of a few parts per billion to a few parts per million, with detection ranges on the order of several kilometers. As an example, Fig. 6 shows time-averaged CC DIAL data obtained for the remote sensing of CO emitted by automobiles at a range of 500 m with a tunable CO_2 laser DIAL system (*22*). The increase in CO concentration during the morning, lunch, and evening rush hours is evident. The sensitivity of the DIAL measurement was approximately 10 ppb and the temporal resolution was approximately 1 second; the CO emission from individual vehicles was easily observed.

Range-resolved DIAL measurements provide a continuous signal as a function of range, based on the backscatter from atmospheric aerosols and particulates. As such, RR DIAL measurements have a significant advantage over CC DIAL measurements in that they can provide a three-dimensional map of the measured species. The major difficulty with RR DIAL is the relatively small backscatter coefficient for atmospheric aerosols and particulates compared to that for

Table 2. Selected list of atmospheric constituents and parameters measured by lidar. Accuracy and ranges given are typical values and depend upon individual lidar measurements.

Constituent or parameter	Laser type	Accuracy	Lidar type	Range (km)
Dust, clouds, volcanic ash, smoke plumes	Ruby, Nd:YAG	1 to 10%	Atmospheric backscatter	10 to 50
H_2O, O_3, SO_2, NO, NO_2, N_2O, C_2H_4, CH_4, HCl, CO, Hg, SF_6, NH_3, CO_2	Dye, CO_2, OPO,* excimer, Co:MgF_2	Variable, 1 ppb to 100 ppm	DIAL, Raman	1 to 5
OH, Na, K, Li, Ca, Ca^+	Dye	10^2 to 10^7 atoms per cubic centimeter	Fluorescence	1 to 90
Temperature, pressure	Dye, Nd:YAG	1 K, 5 mbar	DIAL, Raman	1 to 30
Wind speed	CO_2	0.5 m/sec	Doppler	15

*OPO, optical parametric oscillator.

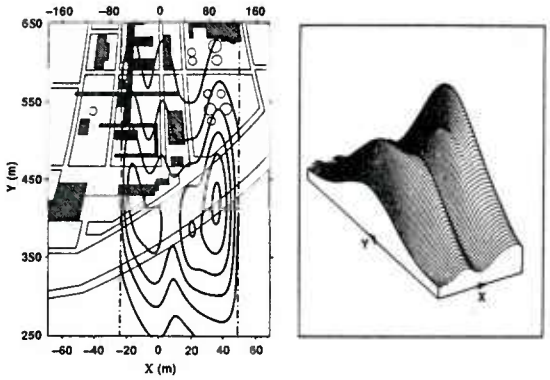

Fig. 7. Illustrations of the laser remote sensing of the concentration of ethylene near the distillation towers of a refinery. (**Left**) Isobars of concentration in increments of 20 ppb. (**Right**) Corresponding three-dimensional plot showing a peak concentration of approximately 150 ppb. [Adapted from (*27*)]

a hard target. Because of the small backscarter coefficients, most RR DIAL measurements have used relatively high-power lasers, or sophisticated optical detection techniques such as photon counting or heterodyne detection to increase sensitivity to the backscartered signal. In spite of these difficulties, several RR DIAL measurements of atmospheric molecules have been made. These measurements include the detection and mapping of SO_2 and NO_2 in a power plant plume (*5*), SO_2 and O_3 near urban centers (*23*), and NO_2 emitted by a chemical factory (*24*). Other examples are atmospheric temperature and pressure measurements based on absorption lines of oxygen near 760 nm (*25*) and precision measurements of O_3 in the upper atmosphere (*26*). These O_3 measurements are particularly important in light of the recent discovery of a "hole" in the atmospheric O_3 layer near Antarctica and the anticipated use of a similar DIAL system by NASA to study this phenomenon.

Finally, as an example of RR DIAL measurements, Fig. 7 shows data obtained by Rothe using a CO_2 laser DIAL system (*27*) which measured the concentration of ethylene (C_2H_4) over the area of a refinery. This figure illustrates the three-dimensional mapping capability of such a system.

Fluorescence lidar. In a fluorescence lidar system, the laser is tuned to an absorption line of the species that is to be measured and the reradiated fluorescence is detected by selective spectral filtering of the returned radiation. The fluorescence radiation may be at the same wavelength as the excitation wavelength or may be red-shifted (have a longer wavelength). In the larter case, a spectrometer or narrow-band interference filter is usually used to reject the strong Rayleigh backscarter and thus detect only the fluorescence signal. The backscatter coefficient for fluorescence is much greater in the UV than in the IR (Table 1); this is due to the combined effects of absorption cross section (greater in the UV than the IR) and radiative lifetime (longer in the IR than in the UV, which permits increased de-excitation due to collisions with ambient molecules).

Several factors that limit the application of fluorescence lidar for remote sensing include problems involving detector sensitivity coupled with solar background radiation, which generally reduces fluorescence measurements for remote sensing to nighttime investigations and to wavelengths shorter than 1 μm, where photomultiplier detection may be used. In addition, at tropospheric pressures an excited molecule will normally undergo several collisions with other molecules before fluorescent emission. This quenching of the excited molecule severely reduces the fluorescent output, rendering it extremely inefficient for most remote sensing applications in the troposphere or even in the lower stratosphere.

In spite of these difficulties, several successful measurements of trace atmospheric species have been made with this technique. Ground-based visible fluorescence lidar systems have been developed by Megie (*28*) and by Gardner and his colleagues (*29*) and have been used to study alkali metal (sodium, potassium, lithium, calcium, Ca^+) concentration profiles at altitudes of 80 to 100 km (*5, 28, 29*). Peak sodium concentrations of about 10^3 to 10^4 atoms per cubic centimeter have been measured in the upper atmosphere; potassium concentrations, about an order of magnitude lower, and lithium atoms, with peak concentrations of approximately 1 atom per cubic centimeter at altitudes near 100 km, have been observed. The return signal from sodium atoms is sufficient to serve as a tracer to study temperature, eddy diffusion, and the dynamics of the wavelike features believed to be due to internal gravity waves and tidal effects in the upper atmosphere.

Another significant application of fluorescence lidar involves the study of the hydroxyl free radical, OH. Although OH occurs as a trace species at very low concentrations (on the order of 0.1 part per trillion), it plays an important catalytic role in various atmospheric chemistry processes and, together with chlorine and nitrogen oxides, is involved in the O_3 destruction cycle in the atmosphere. Airborne measurements of OH have been made with a laser operating at 282 nm (*30*). Concentrations on the order of 10^6 to 10^7 OH per cubic centimeter were observed, corresponding to approximately one part in 10^{13}. These measurements complement the extensive investigation of OH in the stratosphere in which a laser induced fluorescence spectrometer was mounted on a balloon-borne platform (*31*).

Raman scattering lidar. The use of Raman scartering methods for remote sensing is severely limited by the small optical interaction strength for Raman scartering. As a result, this technique is generally used with high-energy pulsed lasers, is restricted to the UV or visible regions of the spectrum so that sensitive photomultiplier tubes can be used for detection, and is most useful for the detection of species either at close range or in high concentration in the atmosphere such as N_2, O_2, and H_2O. It has a range capability of tens of kilometers for the detection of atmospheric N_2 but is limited to about a few hundred meters for pollution monitoring. In addition, its sensitiviry is low (on the order of 100 ppm) as compared with other techniques. Despite these shortcomings, Raman scartering has several features that have made it a useful remote sensing tool. Its most noteworthy feature is that the laser wavelength does not have to be tuned across an absorption line since the spectral information is given by the frequency shift of the emission, which is independent of the laser wavelength. The strength of the scartering, except in certain resonance regions, is only weakly dependent on laser wavelength, and therefore Raman lidar does not require a particular laser frequency as long as the one chosen is effectively free of atmospheric interference.

The Raman-scattered wavelength-shifted spectra are distinct for each molecular species, which allows separate analysis of the Raman returns from each species. This spectral discrimination can be used to advantage by comparing the relative intensity of the returns from the molecule that is being detected to the intensity from atmospheric N_2, whose concentration is known. This ratio approach simplifies a Raman lidar measurement by eliminating atmospheric or instrumental uncertainties in the lidar equation.

A wide variety of Raman lidar measurements of atmospheric polluting species have been made in regions where their concentrations are quite high. Reviews of such measurements are given by Inaba and Kobayashi (*32*), who discuss Raman lidar measurements of SO_2, NO, CO, H_2S, C_2H_4, CH_4, and H_2CO present in high

concentration (100 to 1000 ppm) in oil smoke plumes and automobile exhausts, at ranges on the order of 30 to 100 m. Another application of Raman lidar arises from the fact that the backscattered Raman intensity for a given rotational band is strongly temperature dependent. This property has been used for the remote measurement of atmospheric temperature profiles at ranges of over 2 km with an uncertainty of less than ±2 K. These results are described in a review by Cooney of the use of Raman scattering for the remote sensing of meteorological properties (*33*). In recent Raman lidar experiments, researchers have also studied water vapor profiles near the water-atmosphere boundary layer, subsurface ocean temperature profiles, and ocean turbidity. Long-range (30 km) measurements of atmospheric temperature by means of Raman lidar have also been reported (*15, 34*).

Doppler lidar. Doppler shifts in the return lidar signals have been used to measure wind velocities and to differentiate between molecular and aerosol returns in the atmosphere. Although these shifts are small (a fractional change in frequency of approximately 10^{-8} for a velocity of 1 m/sec at a wavelength of 10 μm), they can be measured by optical heterodyne detection techniques. Heterodyne detection involves the optical mixing of the lidar return with another laser operating at or near the lidar transmitter wavelength, with detection of the difference or beat frequency of the mixed signal.

Most Doppler lidar measurements have used 10-μm CO_2 lasers because CO_2 lasers offer high power and stable single-frequency operation (*35–36*). A review of work in this area, including a large bibliography, has been given by Bilbro (*35*). Recently, Hall and coworkers at NOAA used a CO_2 Doppler lidar to measure the velocity and direction of atmospheric wind fields at ranges up to 12 km (*37*). This system has yielded information on boundary layer flow near storm gust fronts and wind shears near airports; Fig. 8 shows a plot of wind speed and direction measured with Doppler lidar near Denver-Stapleton Airport during a storm, showing the presence of a wind shear–microburst (*38*). Doppler lidar systems have also been used to measure aircraft vortices and clear air turbulence. In particular, an airborne CO_2 laser system based at the NASA Marshall center has been used to construct two-dimensional vector wind fields in the vicinity of the aircraft in flight (*39*).

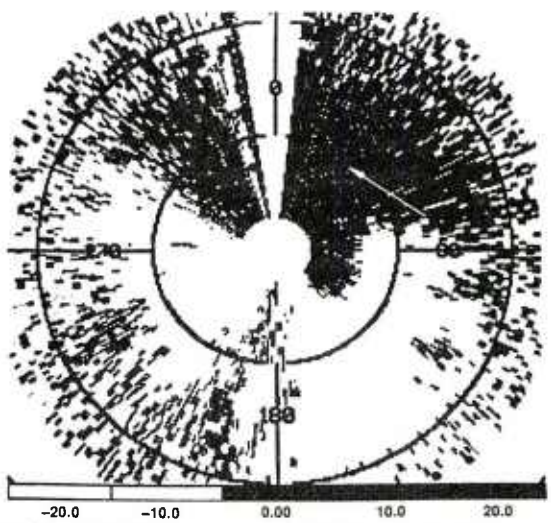

Fig. 8. Doppler lidar measurement of wind direction and velocity near Denver-Stapleton Airport during a storm; the arrow points to the presence of a strong, localized downburst-gustfront. [Adapted from (*38*)]

Doppler broadening effects have also been used by a University of Wisconsin group (*40*) to separate backscattered lidar signals into molecular and aerosol components. This distinction can be made because the Doppler broadening due to the thermal motion of molecules is about two orders of magnitude larger than that of the heavier aerosols. The separation is achieved by using a high-spectral-resolution Fabry-Perot optical interferometer to separate the Doppler-shifted molecular and nearly unshifted aerosol lidar returns. The system has been used in an aircraft to measure optical depth profiles and separate values of the molecular and aerosol backscatter cross sections as a function of height to an altitude of 1.6 km.

Accuracy Limitations

The accuracy of a lidar measurement is limited to the accuracy with which the average value of the lidar returns can be determined, and is therefore influenced by the statistical fluctuations of the lidar signals. These fluctuations are caused by several factors, including detector noise, changes in the propagation and attenuation characteristics due to atmospheric turbulence, changes in the geometry of the lidar beam and target, and variability in the laser power and wavelength. The limitations imposed by detector noise and signal fluctuations appear to be the dominant factors determining lidar measurement accuracy (*20*).

The noise level of the optical detector determines, in part, the accuracy or sensitivity of the lidar system; the lidar return signal must be greater than this noise level to be measured with precision. The ratio of the lidar signal strength and the noise of the system may be expressed analytically by noting that for a direct-detection lidar with a photodiode used for detection of the optical returns, the detector voltage signal-to-noise (*S/N*) ratio is given by (*5, 41*)

$$S/N = \frac{C P_r}{[D(P_r + P_B) + I_O + I_E]^{1/2}} \qquad (6)$$

where P_B is the noise associated with the background radiation power incident on the detector, I_O is the dark current of the detector, I_E is the equivalent noise current of the detector preamplifier, and C and D are constants related to the signal bandwidth, optical wavelength, and detector quantum efficiency. A similar equation may be written for heterodyne detection, modified to include a local oscillator power term, and for optical detection with a photomultiplier tube or avalanche photodiode to include internal gain (*6, 41*). The denominator in Eq. 6 is associated with the shot noise of the system and is due to quantum fluctuations of the signal and noise currents. As expected, the *S/N* ratio for different types of lidar systems will depend on the noise characteristics of the optical detector and on the spectral filtering used in the system. It is often possible to choose a detector so that only one noise term in Eq. 6 is dominant; in this case, one can classify the detection process as being limited by the individual dominant noise source, such as signal shot noise, background noise, or amplifier noise. Optical detection in the UV, visible, and near IR (wavelengths up to 1 μm) uses photomultiplier tubes that have, under optimal conditions, exceptionally low noise levels, are capable of detecting a single photon of light, and are essentially shot noise–limited. Optical detection in the middle IR (1 to 10 μm) usually uses semiconductor materials for direct detection of the optical radiation; these devices are often background noise–limited and have noise levels that are several orders of magnitude higher than photomultiplier tube noise levels. Enhanced detection in the middle IR can be accomplished with optical heterodyne detection, which is capable of single photon detection, but only with a considerable increase in lidar complexity due to the addition of another laser used for optical mixing with the

lidar returns and, in the case of a DIAL system, the precision tunability and tracking of these laser wavelengths.

The accuracy of a lidar measurement is related to the lidar *S/N* ratio shown in Eq. 6 as $\sigma_0 = (S/N)^{-1}$, where σ_0 is the normalized statistical standard deviation of the fluctuating lidar returns and is a measure of the uncertainty in the estimate of the average value of the returns (*41*). It is well known that the accuracy of a measurement can be enhanced by signal averaging and that the *S/N* ratio or accuracy will increase as the square root of the number of pulses integrated. This may be expressed analytically as $\sigma_n = \sigma_0/n^{1/2}$, where σ_n is the standard deviation in the estimate of the mean value of the n pulses. This $n^{1/2}$ improvement in accuracy by signal averaging can be anticipated only if the measured returns from successive signals are uncorrelated, which means that the statistical properties of all the terms in Eq. 6 be temporally random (stochastic). In many lidar examples, the dominant noise sources are random and an $n^{1/2}$ improvement is observed. Such lidar measurements include, as examples, Raman and fluorescence lidar measurements of the upper atmosphere, DIAL measurements when atmospheric attenuation fluctuations are negligible, and the reduction of speckle (interference) effects in Doppler lidar measurements.

In some lidar measurements, however, the fluctuations observed are not random and are caused by long-term variability in the optical properties and attenuation of the atmosphere during the measurement period. This is often seen in DIAL measurements of the atmosphere, especially when the laser beam is transmitted in the lower atmosphere so that it is most susceptible to the influence of long-term drifts in the composition and temperature of the atmosphere near the surface of the earth. Under these conditions the statistical distribution and temporal characteristics of the terms in Eq. 6 are subject to both random and nonrandom influences, and a deviation from the expected $n^{1/2}$ improvement in the *S/N* ratio or σ_n is observed (*42*). An example of this effect is presented in Fig. 9, which shows a logarithmic plot of σ_n as a function of n, the number of lidar pulses averaged, for DIAL data obtained with a CO_2 laser; for comparison, a $n^{1/2}$ improvement is shown as the straight line in the figure. The marked deviation from $n^{1/2}$ behavior shown in Fig. 9 indicates the extent to which nonrandom processes may reduce the effectiveness of signal averaging. Figure 9 is only one example of this observed phenomenon; in fact, the deviation from $n^{1/2}$ behavior ranges from zero to values significantly greater than that shown. The physical sources of the correlation are believed to be atmospheric turbulence and long-term drifts, which lead to temporal changes in atmosphere attenuation during the measurement interval. Both of these effects would produce nonrandom fluctuations in the atmospheric attenuation, α, and thus influence the statistical properties of P_r.

In order to better understand the data shown in Fig. 9, we made a theoretical analysis to quantify the effect of correlation on a statistical ensemble of data, with direct application to DIAL (*43*). This analysis showed that the inclusion of correlation changes the simple $n^{-1/2}$ dependence of σ_n to

$$\sigma_n = \frac{\sigma_0}{n^{1/2}}\left[1 + 2\sum_{j=1}^{n-1}(1 - j/n)\rho_j\right]^{1/2} \quad (7)$$

where ρ_j is the temporal autocorrelation coefficient for a delay time $j\tau$, and τ is the time interval between successive lidar measurements. For stochastic data, ρ_j is zero and Eq. 7 reduces to the $n^{-1/2}$ form as expected. As seen in Eq. 7, the effect of a nonzero value of ρ_j is to reduce the improvement in signal averaging. Further DIAL experiments (*43*) have shown that Eq. 7 is in excellent agreement with the observed DIAL data as presented in Fig. 9.

Equation 7 can be shown to reduce to $\sigma_n = \sigma_0 \rho_j^{1/2}$ for large n and nonzero ρ_j. This result shows that a limit exists, independent of n, for the improvement in the accuracy of a lidar measurement if nonrandom changes occur in the atmosphere during the measurement interval (*43*). Equation 7 is valid, in general, for all experimental measurements and describes quantitatively the often-observed diminished improvement from long-term averaging when nonrandom perturbations are causing changes in the average signal during the measurement period.

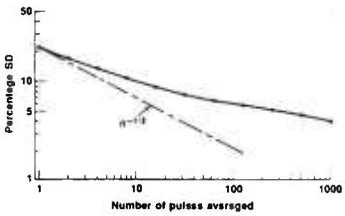

Fig. 9. Measurement accuracy (percent standard deviation) of CO_2 lidar signal returns from a diffusely reflecting target at a range of 2.7 km as a function of the number of pulses averaged. The reduced accuracy improvement relative to $n^{-1/2}$ behavior is due to long-term drifts in atmospheric attenuation.

Finally, while Eq. 7 does predict the increase in accuracy of a lidar measurement through signal averaging, σ_n can be reduced by techniques that reduce either the initial values of σ_0 or the initial value of the correlation coefficient. These techniques (*43–45*) include the use of very high repetition rate lasers to increase the number of lidar samples collected before the atmosphere changes appreciably; the use of dual, nearly simultaneously transmitting, lasers for DIAL experiments; and the use of laser wavelength agility. Even with some of these techniques, the accuracy of most current lidar experiments has been limited to values on the order of a percent (that is, $\sigma_n \approx 1\%$) under optimal conditions and to values on the order of 1 to 10% under normal atmospheric conditions.

Future Directions

Laser remote sensing is a useful tool for probing the composition and physical state of the atmosphere and, by means of single-ended measurements at a distance, permits measurements at locations that cannot be reached with conventional detection methods such as chemical or optical point sensors. Although technical limitations do exist, in many instances, lidar offers the only realistic measurement technique that can detect a physical quantity and produce a three-dimensional map of the quantity in real time.

The future of laser remote sensing appears to be quite promising and is dependent upon factors that include (i) the development of practical, new, eye-safe laser sources that cover the spectral gaps shown in Fig. 4, (ii) further reduction of lidar system complexity, cost, and size, and (iii) the future use of lidar techniques in new applications. Among the latter are several emerging industrial and medical applications that include the use of fiber optics in enclosed or hostile environments, the use of airborne lidars for oil, gas, and geological exploration, and the exploitation of the long-range (>100 km) detection capability and wide surveillance potential of space-borne laser remote sensing. Examples that are currently being explored include (i) the detection of methane gas leaks in a coal mine with a diode laser lidar system, (ii) the use of a laser coupled to a low-loss optical fiber network to detect methane or natural gas leaks in an industrial processing plant, (iii) the Doppler lidar measurement of global wind fields from a satellite to increase the accuracy of weather forecasts, and (iv) the planned use of lidar aboard the NASA space-borne Earth Observing System for global temperature, water vapor, and pressure measurements.

REFERENCES AND NOTES

1. A. I. Carswell, *Can. J. Phys.* 61, 378 (1983).
2. H. Kildal and R. Byer, *Proc. IEEE* 59, 1644 (1971).
3. R. Byer, *Opt. Quantum Electron.* 7, 147 (1975).
4. E. D. Hinkley, Ed., *Laser Monitoring of the Atmosphere* (Springer-Verlag, Berlin, 1976).
5. D. K. Killinger and A. Mooradian, Eds., *Optical and Laser Remote Sensing* (Springer-Verlag, Berlin, 1983).
6. R. M. Measures, *Laser Remote Sensing: Fundamentals and Applications* (Wiley, New York, 1984).
7. L. D. Smullin and G. Fiocco, *Nature (London)* 194, 1267 (1962); G. Fiocco and L. D. Smullin, *ibid.* 199, 1275 (1963).
8. M. G. H. Ligda, in *Proceedings of the 1st Conference on Laser Technology*, U.S. Navy ONR (1963), pp. 63–72.
9. R. M. Schotland, in *Proceedings of the 4th Symposium on Remote Sensing of the Environment*, 12 to 14 April 1966, University of Michigan, Ann Arbor, p. 273.
10. E. D. Hinkley and P. L. Kelley, *Science* 171, 635 (1971).
11. W. Driscoll and W. Vaughan, Eds., *Handbook of Optics* (McGraw-Hill, New York, 1978); H. W. Yates and J. H. Taylor, *Infrared Transmission of the Atmosphere* (Report 5453 AD 240188, U.S. Naval Research Laboratory, Washington, DC, 1960).
12. The values for ρ shown in Table 1 for atmospheric species were derived with a range resolution, ΔR, of 100 m and the simplifying assumption of isotropic scattering. For the case of Rayleigh, Mie, and Raman scattering, the effective reflectivity, ρ, is related to the volume backscatter coefficient and thus to the extinction coefficient, α, for each individual interaction. For the case of absorption, as noted in the text, the value of ρ corresponds to backward-directed fluorescence emission of the atom or molecule after it has absorbed the incident light. For atmospheric species, this fluorescence process is efficient in the UV and visible part of the spectrum but suffers considerably in the IR because of collisional quenching with other atmospheric molecules during the long lifetime of an IR transition.
13. *Laser Focus Buyers Guide* (Penn Well, Tulsa, OK, 1986), pp. 47–133.
14. *Tunable Solid State Lasers—Technical Digest* (topical meeting, Optical Society of America, 16 and 17 May 1985, Washington, DC) (Optical Society of America, Washington, DC, 1985).
15. *Eleventh International Laser Radar Conference* (Conference Publication 2228, NASA, Washington, DC, 1982); *Twelfth International Laser Radar Conference Proceedings* (Aix-en-Provence, 1984); *Optical Remote Sensing of the Atmosphere—Technical Digest* (Optical Society of America, Washington, DC, 1985); *Optical Techniques for Remote Probing of the Atmosphere—Technical Digest* (Optical Society of America, Washington, DC, 1983). Several papers based on submissions at these conferences have been published in *Appl. Opt.* 22, 2527 (1983); *ibid.*, p. 3684; *ibid.* 24, 3443 (1985).
16. M. P. McCormick, *Opt. Eng.* 21, 340 (1982); ——— and T. J. Swissler, *Geophys. Res. Lett.* 10, 877 (1983).
17. E. E. Uthe *et al.*, *Bull. Am. Meteorol. Soc.* 61, 1035 (1980).
18. P. Chýlek, G. W. Grams, R. G. Pinnick, *Science* 193, 480 (1976); J. Heintzenberg, J. H. Muller, H. Quenzel, E. Thomalla, *Appl. Opt.* 20, 1308 (1981).
19. G. W. Kattawar and G. N. Plass, *Appl. Opt.* 15, 3166 (1976).
20. N. Menyuk and D. K. Killinger, *ibid.* 22, 2690 (1983).
21. W. B. Grant and R. T. Menzies, *J. Air Pollut. Control Assoc.* 33, 187 (1983).
22. D. K. Killinger, N. Menyuk, W. E. DeFeo, *Appl. Phys. Lett.* 36, 402 (1980).
23. E. V. Browell, *Opt. Eng.* 21, 128 (1982).
24. K. W. Rothe, U. Brinkman, H. Walther, *Appl. Phys.* 4, 181 (1974).
25. C. L. Korb and C. Y. Weng, *Appl. Opt.* 22, 3759 (1983).
26. J. Werner, K. W. Rothe, H. Walther, *Appl. Phys. B* 32, 113 (1983); O. Uchino, M. Tokunaga, M. Maeda, Y. Miyozoe, *Opt. Lett.* 8, 347 (1983).
27. K. W. Rothe, *Radio Electron. Eng.* 50, 567 (1980).
28. G. Megie, F. Bos, J. E. Blamont, M. L. Chanin, *Planet. Space Sci.* 26, 27 (1978).
29. J. R. Rowlett, C. S. Gardner, E. S. Richrer, C. F. Sechrist, *Geophys. Res. Lett.* 5, 683 (1978).
30. C. C. Wang, L. I. Davis, Jr., P. M. Selzer, *J. Geophys. Res.* 86, 1181 (1981); D. D. Davis, W. Heaps, T. McGee, *Geophys. Res. Lett.* 3, 331 (1976).
31. J. G. Anderson, *Geophys. Res. Lett.* 3, 165 (1976); W. S. Heaps, *Appl. Opt.* 19, 243 (1980); ——— and T. J. McGee, *J. Geophys. Res.* 90, 7913 (1985).
32. H. Inaba and T. Kobayashi, *Opto-electronics* 4, 101 (1972); H. Inaba, in (*4*), chap. 5.
33. J. A. Cooney, *Opt. Eng.* 22, 292 (1983).
34. S. H. Melfi and D. Whiteman, *Bull. Am. Meteorol. Soc.* 66, 1288 (1985); D. A. Leonard, *Opt. Eng.* 20, 91 (1981); F. E. Hoge and R. N. Swift, *Appl. Opt.* 22, 3778 (1983); S. H. Melfi and D. Whiteman, in *Proceedings of the 13th International Laser Radar Conference* (Conference Publication 2431, NASA, Washington, DC, 1986), p. 188.
35. J. W. Bilbro, *Opt. Eng.* 19, 533 (1980).
36. R. Teosre and R. N. Capes, *J. Appl. Meteorol.* 17, 1575 (1978).
37. F. F. Hall, Jr., *et al.*, *Appl. Opt.* 23, 2503 (1984).
38. R. M. Hardesty, K. Elmore, M. E. Jackson, in *21st Conference on Radar Meteorology* (American Meteorological Society, Boston, 1983).
39. J. Bilbro, G. Fichtl, D. Fitzjarrald, M. Krause, R. Lee, *Bull. Am. Meteorol. Soc.* 65, 348 (1984).
40. S. T. Shipley *et al.*, *Appl. Opt.* 22, 3716 (1983); *ibid.*, p. 3725.
41. This equation refers to the definition for *S/N* ratio used in communication theory. A more general definition of lidar *S/N* includes the concept of carrier-to-noise ratio and the effects of target speckle and atmospheric turbulence. See, for example, J. H. Shapiro, B. A. Capron, R. C. Harney, *Appl. Opt.* 20, 3292 (1981).
42. D. K. Killinger and N. Menyuk, *IEEE J. Quantum Electron.* QE-17, 1917 (1981); ———, W. E. DeFeo, *Appl. Opt.* 22, 682 (1983).
43. N. Menyuk, D. K. Killinger, C. R. Menyuk, *Appl. Opt.* 21, 3377 (1982); *ibid.* 24, 118 (1985).
44. B. J. Rye, *J. Appl. Meteorol.* 22, 1899 (1983).
45. R. C. Harney, *Appl. Opt.* 22, 3747 (1983).

46. This work was supported by the National Aeronautics and Space Administration and the Air Force Engineering and Services Center.

REPORT DOCUMENTATION PAGE

1a. REPORT SECURITY CLASSIFICATION Unclassified	1b. RESTRICTIVE MARKINGS
2a. SECURITY CLASSIFICATION AUTHORITY	3. DISTRIBUTION/AVAILABILITY OF REPORT Approved for public release; distribution unlimited.
2b. DECLASSIFICATION/DOWNGRADING SCHEDULE	
4. PERFORMING ORGANIZATION REPORT NUMBER(S) LRS Final Report	5. MONITORING ORGANIZATION REPORT NUMBER(S) ESD-TR-87-028 ESL-TR-85-039
6a. NAME OF PERFORMING ORGANIZATION Lincoln Laboratory, MIT 6b. OFFICE SYMBOL *(If applicable)*	7a. NAME OF MONITORING ORGANIZATION Electronic Systems Division
6c. ADDRESS *(City, State, and Zip Code)* P.O. Box 73 Lexington, MA 02173-0073	7b. ADDRESS *(City, State, and Zip Code)* Hanscom AFB, MA 01731
8a. NAME OF FUNDING/SPONSORING ORGANIZATION Engineering and Services Laboratory 8b. OFFICE SYMBOL *(If applicable)*	9. PROCUREMENT INSTRUMENT IDENTIFICATION NUMBER Program 245
8c. ADDRESS *(City, State, and Zip Code)* Air Force Engineering and Services Center Tyndall AFB, FL 32403	10. SOURCE OF FUNDING NUMBERS PROGRAM ELEMENT NO.: 63723F, 63745F PROJECT NO.: 1900 TASK NO.: WORK UNIT ACCESSION NO.:
11. TITLE *(Include Security Classification)* Laser Remote Sensing of Atmospheric Pollutants	
12. PERSONAL AUTHOR(S) Dennis K. Killinger, Norman Menyuk, and Aram Mooradian	
13a. TYPE OF REPORT Final Report 13b. TIME COVERED FROM 10/1/84 TO 9/30/85	14. DATE OF REPORT *(Year, Month, Day)* 30 September 1985 15. PAGE COUNT 58
16. SUPPLEMENTARY NOTATION None	

17. COSATI CODES		
FIELD	GROUP	SUB-GROUP

18. SUBJECT TERMS *(Continue on reverse if necessary and identify by block number)*

laser remote sensing
environmental monitoring
differential absorption lidar (DIAL)
CO_2 and Co:MgF_2 DIAL systems
hydrogen chloride

19. ABSTRACT *(Continue on reverse if necessary and identify by block number)*

This is the FY85 Final Report on the program entitled "Laser Remote Sensing of Atmospheric Pollutants" supported by the Air Force Engineering and Services Center.

The specific tasks which were conducted during FY85 for this research program consisted of the following: (a) The continuation of the Co:MgF_2 DIAL measurement of atmospheric species, and (b) initial remote sensing demonstration of a HCl plume in the atmosphere. Each of these tasks is described in detail in a following sections. Supportive documentation is included in the appendices.

20. DISTRIBUTION/AVAILABILITY OF ABSTRACT ☐ UNCLASSIFIED/UNLIMITED ☒ SAME AS RPT. ☐ DTIC USERS	21. ABSTRACT SECURITY CLASSIFICATION Unclassified
22a. NAME OF RESPONSIBLE INDIVIDUAL Maj. Thomas J. Alpert, USAF	22b. TELEPHONE *(Include Area Code)* (617) 863-5500, Ext. 2330 22c. OFFICE SYMBOL ESD/TML